



UNIVERSITÀ
DEGLI STUDI
DI PADOVA



DIPARTIMENTO
DI INGEGNERIA
DELL'INFORMAZIONE

MASTER'S DEGREE IN ELECTRONIC ENGINEERING

Effect of Vibration on Expected Life of IGBT Modules

CANDIDATE

Francesco Rigo

Student ID 2080479

DATE

04/09/2024

SUPERVISOR

Prof. Gaudenzio Meneghesso

University of Padova

CO-SUPERVISORS

Prof. Francesco Iannuzzo

Prof. Amir Sajjad Bahman

University of Aalborg

ACADEMIC YEAR
2023/2024

Copyright © Aalborg University 2024

The software utilized in this thesis includes ANSYS Student 2024 R1, SolidWorks, Rhinoceros 3D 8, MATLAB, KiCAD, and Arduino IDE. The drawings have been entirely hand-drawn or prepared through Canva and Biorender, except for the ones which report a reference citation.

Acknowledgments

English

I would like to express my gratitude to my advisors Francesco Iannuzzo, Amir Sajjad Bahman, and Gaudenzio Meneghesso for their support over these months. Their guidance has been fundamental to my academic journey and the completion of this work. I also want to thank Soroush Ahooye Atashin and Kaichen Zhang, who have been crucial to the development of my thesis.

I thank my family and grandparents. Since I was a child, they have always inspired and encouraged me to study.

I thank Sofia, who has been by my side every day over these years. Her constant presence and support have helped me overcome difficult moments and stay focused on my goals.

Finally, I would like to thank my friends, both those from Villa Bartolomea and those I met at the Universities of Padua and Aalborg. Their company has been a source of happiness for me.

Italian

Vorrei esprimere la mia gratitudine ai miei relatori Francesco Iannuzzo, Amir Sajjad Bahman e Gaudenzio Meneghesso, per avermi affiancato con passione e dedizione durante questi mesi. La loro guida è stata fondamentale per il mio percorso accademico e per la realizzazione di questo lavoro. Insieme a loro voglio ringraziare Soroush Ahooye Atashin e Kaichen Zhang che sono stati fondamentali per lo svolgimento della tesi.

Ringrazio la mia famiglia e i miei nonni. Sin da quando ero piccolo, mi hanno sempre ispirato e incoraggiato a studiare. La loro costante fiducia in me è stata una fonte inesauribile di motivazione.

Ringrazio Sofia, che mi è stata vicino ogni giorno in questi anni. La sua presenza costante ed il suo sostegno mi hanno aiutato a superare i momenti difficili e a rimanere concentrato sui miei obiettivi.

Infine, vorrei ringraziare i miei amici, sia quelli di Villa che quelli conosciuti alle Università di Padova e di Aalborg. La loro compagnia è stata per me motivo di svago e di serenità.

Abstract

English

This study assesses the reliability of Insulated Gate Bipolar Transistor (IGBT) modules exposed to mechanical vibrations typical in electric vehicles and industrial electronics. The effects of varying vibration frequencies and amplitudes on the Expected Life of IGBT modules are evaluated, mainly focusing on crack failures. Using Finite Element Analysis (FEA), critical stress points that contribute to mechanical failures are identified. Results show a significant correlation between failure rates and vibration profiles, especially at frequencies near the resonant frequency of bond wires, which notably accelerate fatigue. Recommendations to improve mechanical stability are provided, enhancing the durability and reliability of IGBT modules in vibration-intensive environments. This research offers key insights for power electronics manufacturers and designers.

Italian

Questo studio valuta l'affidabilità dei moduli Insulated Gate Bipolar Transistor (IGBT) esposti a vibrazioni meccaniche tipiche nei veicoli elettrici e nell'elettronica industriale. Vengono valutati gli effetti delle variazioni di frequenza e ampiezza delle vibrazioni sulla vita attesa dei moduli IGBT, con un'attenzione particolare ai guasti dovuti a crepe. Utilizzando l'Analisi agli Elementi Finiti (FEA), vengono identificati i punti di stress critici che contribuiscono ai guasti meccanici. I risultati mostrano una significativa correlazione tra i tassi di guasto e i profili di vibrazione, specialmente a frequenze vicine alla frequenza di risonanza dei fili di collegamento, che accelerano notevolmente la fatica. Vengono fornite raccomandazioni per migliorare la stabilità meccanica, aumentando la durata e l'affidabilità dei moduli IGBT in ambienti soggetti a forti vibrazioni. Questa ricerca offre approfondimenti chiave per i produttori e i progettisti di elettronica di potenza.

Summary

This master's thesis project targets the reliability analysis of Insulated Gate Bipolar Transistor (IGBT) modules when subjected to vibrational stresses, addressing a notable research gap. Initially, a comprehensive literature review indicates that cracks at the feet of bond wires are the primary failure mechanism for IGBT modules under vibrational loads. The review also highlights the absence of studies providing an Expected Life trend for these modules.

To address this gap, the thesis explores how random and harmonic vibrations differently influence IGBT modules, particularly focusing on the induced stress on bond wires. The research is segmented into two principal sections: simulation using Finite Element Analysis (FEA) with ANSYS software, and experimental testing.

During the simulation phase, a detailed 3D model of the IGBT module is designed using SolidWorks and Rhinoceros 3D, featuring precise dimensions and material layer thicknesses. This phase extends beyond dimensional accuracy to examine the materials' elasticity and vibration resistance, extracting SN curves for each material to estimate their lifetimes in ANSYS.

A crucial part of the simulation involves applying and comparing the effects of random and harmonic vibrations within ANSYS. The study identifies vibration frequency as a critical parameter. Extensive modal analysis is used to analyze how the shape of bond wires influences the stress near their feet. Additionally, a key equation is derived to calculate the first resonance frequency of the bond wires based on their dimensions, aiding in determining the physical requirements of bond wires relative to the vibrational frequencies of their intended operational environments.

The simulation specifically focuses on random vibrations to align with the capabilities of the Typhoon 2.5 machine used in laboratory experiments. A resonator is designed via 3D modeling to narrow the broad frequency range of random vibrations, simplifying the analysis. Simulation results validate the theoretical expectations, showing increased stress and failure probability as the vibration frequency nears the bond wires' first resonance frequency. This underscores the need to adapt bond wire dimensions, particularly their thickness and length, to mitigate resonance within the module's operational environment.

The experimental phase commences with designing a monitoring circuit to assess the integrity of the IGBT module during vibration tests. This circuit utilizes an Arduino DUE

board, LEDs as alert indicators, and BJTs with resistors for driving the IGBTs and diodes, continuously checking all connections' continuity. After assembling the circuit, the module is mounted on top of the resonator, which in turn is fixed on the vibration plate of the Typhoon 2.5. Various excitation frequencies and acceleration levels are tested to evaluate the module's Expected Life under different conditions.

It should be noted that this thesis does not provide an Expected Life characteristic for every possible vibration condition under which the module might operate, due to the infinite combinations of frequencies and accelerations. However, this research enhances understanding of the module's reliability under vibrational loads. Indeed, by employing a resonator to evaluate the Expected Life of the module as a function of vibration frequency (while maintaining constant displacement), it is demonstrated that frequency is the most critical parameter to consider.

Preface

The thesis is drawn up as follows:

- *Chapter 1:* This chapter introduces the thesis and focuses on the initial literature review. It highlights the current state of research regarding the reliability of IGBT modules under vibrational loads and identifies the persistent gaps that this thesis aims to address.
- *Chapter 2:* This chapter provides the necessary background on vibration analysis crucial for conducting reliability studies. It specifically discusses the differences between harmonic and random vibrations and describes some key vibration analysis techniques.
- *Chapter 3:* This chapter lists and explains the material properties essential for conducting a detailed fatigue analysis of the considered module. Understanding these properties is crucial for the subsequent simulations and experiments.
- *Chapter 4:* This chapter details the structure of the IGBT module under study and summarizes the dimensions and thicknesses of all layers, which are critical for accurate simulations. Moreover, each material within the module is analyzed, specifically focusing on deriving each material's Young's modulus, Poisson's ratio, and SN curve.
- *Chapter 5:* This chapter details the setup of the ANSYS simulation environment for conducting a comprehensive vibration reliability study. It also includes a comparative analysis between simple harmonic and random vibrations within this simulation framework. Finally, it outlines the results obtained from the simulations, offering insights on the simulated expected life of the IGBT module.
- *Chapter 6:* This chapter describes how the experimental setup was constructed and discusses the design and functionality of the circuit used to test the integrity of the IGBT module. Finally, it presents the results obtained from the experimental work, with some insights on the properties of silicone gel in improving the IGBT module's bond wires reliability.
- *Chapter 7:* This chapter summarizes the simulation and experimental results, comparing them and explaining their differences and similarities.

Contents

1	Introduction - State of the art	1
2	Vibration Theory and Analysis Techniques	5
2.1	Simple harmonic vibration	5
2.2	Random vibration	6
2.3	Modal analysis	9
2.4	Frequency response analysis	10
3	Mechanical Properties and Fatigue	11
3.1	Mechanical Stress and Strain	11
3.2	Young's modulus and Poisson's ratio	13
3.3	SN Curves and Fatigue	15
4	Case study	19
4.1	Module schematic	19
4.2	Module Internal Structure and Materials Composition	20
4.3	Bond wires' SN curve	21
4.4	Inverter bare dies	23
4.5	Dimensions and thicknesses summary	24
4.6	Final module model	25
5	Vibration simulation in ANSYS	27
5.1	Modal analysis	27
5.2	Harmonic and Random Vibration environments	28
5.3	Fatigue in ANSYS	31
5.4	Resonator design and testing	32
5.5	Modal analysis results	36
5.6	Harmonic and Random Vibration results	41
5.7	Simulated expected life	45

6	Experimental campaign	49
6.1	Equipment description	49
6.2	Module mounting structure	51
6.3	Monitoring circuit	51
6.4	Experimental results	58
7	Results summary	63
8	Conclusion	65
	References	66
	Bibliography	67
A	Control software	71
B	Experimental setup	73
C	Monitoring circuit	77

Chapter 1

Introduction - State of the art

With the growing demand for Insulated Gate Bipolar Transistor (IGBT) modules, understanding their failure mechanisms is becoming increasingly important. Many studies have focused on their reliability under various stressors, such as temperature variations and power cycling. However, the reliability of IGBT modules under vibrational loads continues to be a notable research gap, as only a few studies have thus far explored their failure mechanisms in such environments. To guarantee robust performance across various conditions, it is therefore crucial to deepen the understanding of how these modules respond to such stresses.

The establishment of standard limits for vibrational forces, such as those detailed in ISO 16750-3 [1] for automotive road equipment, has facilitated a more profound understanding of the stresses that IGBT modules need to endure. Environmental vibrations can appear as either simple harmonic or random vibrations. In analyzing random vibrations, the Power Spectral Density (PSD) function, explained in [2], proves to be a critical tool. The PSD function helps in characterizing the vibrational loads during tests. By understanding the PSD limit profile versus vibration frequency from standards, researchers can apply these limits to evaluate specific products under the worst-case vibrational conditions.

Various studies have adopted this approach, including research [3], which utilized Finite Element Analysis for IGBT failure analysis. This study analyzed both simple harmonic and random vibrations. The findings suggest that the stress distribution across the module remains nearly identical in both scenarios. However, elevated stress levels in random vibrations, particularly near the bonding line's foot, heighten the likelihood of device failure (Von Mises stresses equal to 3.17 MPa in simple harmonic and 12.76 MPa in random vibrations).

Further research, such as [4], explored these findings through both hardware simulation and a different software simulation. Studying IGBT modules under horizontal vibration load with frequency $f = 250$ Hz and acceleration $a = 20$ g, the research reveals that, as expected from the previous study, the IGBT cracked at the root of the gate and kelvin-emitter bondwires. COMSOL simulations validated these findings, emphasizing that even slight bond dimension alterations result in stress distribution variations and affect the Number of

Cycles to Failure (NCF) during tests on different IGBTs. The analysis over 5 different IGBT modules reported indeed a high discrepancy between the NCFs of the different samples. This study therefore underscores the critical role of precision in manufacturing processes to mitigate failures induced by vibrational stresses in IGBTs.

Other analysis, not taking into consideration bondwires failures, were carried out as well. For instance, [5] analyzed the reliability of an IGBT module's solder layer under vibrational loads. It was found that, since the first resonant frequency was falling within the random excitation bandwidth, the displacement and induced stresses were significantly higher at that frequency. It was therefore recommended to minimize vibrational loads near the first resonant frequency. Importantly, the analysis also revealed that increasing the substrate thickness tends to prolong the solder layer's life, whereas increasing the substrate width tends to decrease it. The analysis further indicates that an increase in the module volume lowers the structure's fundamental frequency. These findings suggest that, in structural design, strategically increasing the substrate thickness can effectively extend the solder layer's lifespan and enhance the overall reliability of the component.

Moreover, other studies not only focusing on IGBT modules, carried out vibration reliability analysis on electronic devices. For instance, [6] conducted a comprehensive analysis incorporating an electro-mechanical shaker and Laser Doppler Vibrometry (LDV) testing to dynamically and mechanically analyze an IGBT Gate Driver. LDV recorded the modal behavior, providing contactless measurements, and determined the transfer function of the IGBT driver, which was mounted on a vibration shaker. Once derived the transfer functions, fatigue cycle ratios were calculated using Steinberg's Three-Band-Technique and stress-based fatigue curves. Subsequently, an Highly Accelerated Life Test (HALT) was conducted to assess the device's lifetime and potential failure locations. X-Ray computer tomography identified internal structural damage, such as delamination in the DC/DC converter and solder joint separation on the PCB.

Another study [7], through ABAQUS FEA, analyzed the reliability of solder joints in power modules, considering the possibility of varying the vibration loading angles. Specifically, angles of 0° (horizontal excitation), 30° , 45° , 60° , and 90° (vertical excitation) were selected. As the input frequency increased, the solder joints became more susceptible to failure. The primary stress distribution analysis identified the solder joints between MOSFETs and the PCB as the weakest component. The study predicted that an increase in the angle of vibration loading would diminish the possibility of crack initiation and propagation. Indeed, the influence of input frequency on stress was more pronounced at lower loading angles and the system exhibited higher reliability under 90° loading. They finally used Miner's rule to determine the expected life of the device, again demonstrating that the decrease in the angle decreases also the NCF value.

Once obtained a stress distribution across a module, different approaches can be used to derive an prediction on its lifetime.

For example, in their research, [8] conducted a statistical analysis of the failure mechanisms affecting IGBT modules exposed to both mechanical and temperature stresses. They

performed statistical analysis with six set of temperatures and vibrational frequencies. The Shapiro–Wilk test, Weibull and Maximum Likelihood Estimation (MLE) were used to analyze the accelerated life test data of the IGBT modules and estimated that the average service life of the IGBT module is 12.56 years under different environmental conditions.

This thesis aims to consolidate the limited existing literature knowledge by developing a comprehensive 3D model of an IGBT module, focusing particularly on the bond wires design, which are identified as the most likely components to fail. Utilizing detailed Finite Element Analysis and experimental work, the objective is to predict which component will fail first and estimate its time to failure, thereby deriving an Expected Life characteristic for the device.

Chapter 2

Vibration Theory and Analysis Techniques

2.1 Simple harmonic vibration

Simple harmonic vibration refers to the fundamental sinusoidal motion exhibited by vibrating systems. In such oscillatory behavior, key quantities are defined to characterize the motion, namely displacement ($d(t)$), velocity ($v(t)$), acceleration ($a(t)$), and frequency (f). All of these quantities follow a sinusoidal behaviour and can be described as in equation 2.1 and depicted as in Figure 2.1.

$$\begin{aligned}d(t) &= D\sin(\omega t + \phi_d) \\v(t) &= V\sin(\omega t + \phi_v) \\a(t) &= A\sin(\omega t + \phi_a)\end{aligned}\tag{2.1}$$

In an harmonic vibration, the displacement and acceleration values are totally out of phase between each other (i.e., they have a 180° phase shift), while instead the velocity is in quadrature (i.e., 90° phase shift) with the displacement and acceleration values. The amplitudes of the three quantities (D , V and A) are interrelated. Indeed, once one of these values has been established, through the frequency it is possible to derive the two remaining ones. For instance, assuming to firstly define the acceleration, then equation 2.2 holds.

$$\begin{aligned}V &= \frac{A}{2\pi f} \\D &= \frac{V}{2\pi f} = \frac{A}{(2\pi f)^2}\end{aligned}\tag{2.2}$$

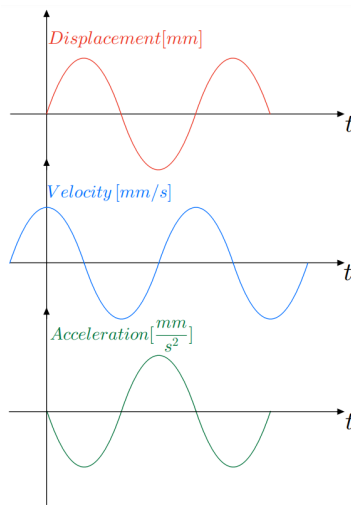


Figure 2.1: Simple harmonic vibration main quantities

2.2 Random vibration

Random vibrations exhibit a distinctive characteristic: their ability to simultaneously engage all frequencies within a structure, unlike sinusoidal functions that are confined to specific frequencies. Random vibrations span a continuous spectrum of frequencies, with both the amplitude and phase of the signal undergoing random fluctuations over time. Such vibrations, found in various applications (e.g., vehicle dynamics), result from a combination of numerous frequencies. Figure 2.2 represents a typical acceleration vs. time characteristic for a random vibration.

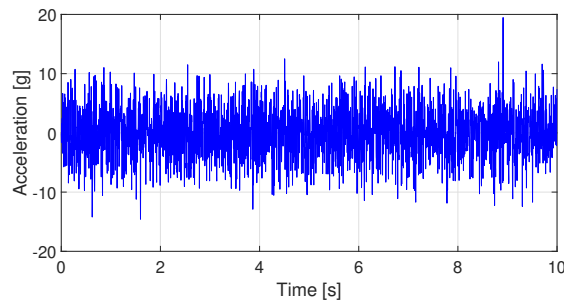


Figure 2.2: Typical random acceleration waveform

In random vibrations, excitations such as displacement, velocity, or acceleration, exhibit statistical rather than deterministic behavior. Such quantities are often assumed to adhere to a Gaussian distribution, which is mathematically defined by a probability density function. Its mean value (μ_x) is assumed to be zero and its the standard deviation (σ_x) represents the variation from the mean. The Gaussian process probability density function is:

$$p(x) = \frac{1}{\sqrt{2\pi}\sigma_x} e^{-\frac{1}{2}\left(\frac{x-\mu_x}{\sigma_x}\right)^2} \quad (2.3)$$

The variance of the process is calculated as follows:

$$\sigma_x^2 = E[(X - E(X))^2] \quad (2.4)$$

For zero mean, the standard deviation is equivalent to the Root Mean Square (RMS) value (which characterizes the signal's intensity over time) since:

$$\sigma_x = \sqrt{\sigma_x^2} = \sqrt{E[(X - E(X))^2]} = \sqrt{E[X^2]} = RMS^2 \quad (2.5)$$

The variance can also be expressed as the zero lag auto-covariance of the process, which is calculated, for zero mean, as:

$$R_x(\tau) = E[(X(t) - E(X)) \cdot (X(t + \tau) - E[X])] = E[X(t) \cdot X(t + \tau)] \quad (2.6)$$

and therefore, given equation 2.5:

$$R_x(0) = \sigma_x^2 \quad (2.7)$$

The auto-covariance is related to the Power Spectral Density through the Fourier Transform, as:

$$\begin{aligned} S_x(f) &= \int_{-\infty}^{+\infty} R_x(\tau) e^{-j2\pi f\tau} d\tau \\ R_x(t) &= \int_{-\infty}^{+\infty} S_x(f) e^{j2\pi ft} df \end{aligned} \quad (2.8)$$

Therefore it goes that:

$$R_x(0) = \int_{-\infty}^{\infty} S_x(f) df = \sigma_x^2 \quad (2.9)$$

And finally:

$$\sigma_x = RMS = \sqrt{\int_{-\infty}^{\infty} S_x(f) df} \quad (2.10)$$

This integral represents the distribution of signal power across different frequencies, providing a measure of the total power contained within the signal. This highlights the importance of Power Spectral Density in delineating the statistical attributes of random vibrations, as it offers a simplified approach to determining the RMS value of the signal. The relation between the Power Spectral Density value and the RMS one is fundamental to understand what follows in the next chapters, for the description of the input random vibration parameters.

The assumption of ergodicity in the stochastic process ensures that its statistical properties remain constant over time. This assumption facilitates the interpretation of output responses, which often exhibit Gaussian characteristics. These responses are typically divided into regions based on standard deviations. The three key regions are: the 1σ region, which accounts for occurrences 68.3% of the time; the 2σ region, covering occurrences 95.4% of the time; and the 3σ region, including occurrences 99.7% of the time.

The frequency content of the time history vibration signal (i.e., the spectrum), encapsulated in the PSD, is utilized as input in random vibration analysis. Since a vibration signal can be characterized by three fundamental parameters (displacement, velocity, and acceleration), the Power Spectral Density (PSD) can correspond to any of these values. Taking acceleration as an example, the unit of measure for its PSD is given as $\frac{g_{RMS}^2}{Hz}$, where g represents gravitational acceleration. To derive the PSD curve from the time history values, the bandwidth of the random vibration signal needs to be firstly determined. Subsequently, it should be divided into smaller frequency intervals and for each interval, the RMS (Root Mean Square) value of the acceleration versus time characteristic must be calculated using the simple formula (where i indicates the frequency interval index and j the acceleration sample index for each frequency interval and therefore N_i is the number of samples for the interval i):

$$RMS_i = \sqrt{\frac{1}{N_i} \sum_{j=1}^{N_i} a_j^2} \quad (2.11)$$

Once the RMS value for each interval is determined, the following formula applies (where N is the number of frequency intervals and RMS the overall acceleration signal RMS value):

$$RMS = \sqrt{\sum_{i=1}^N RMS_i^2} \quad (2.12)$$

The PSD curve is then constructed by computing the square of each RMS value and dividing it by the respective frequency interval bandwidth. Finally, connecting these constant values through a piecewise linear curve yields the final PSD curve.

In this thesis, a flat PSD curve will be considered, meaning that the power is equally distributed across the operating bandwidth. In this particular example, it is possible to easily relate the acceleration RMS value and the Power Spectral Density one through the simple

formula:

$$PSD = \frac{s_{RMS}^2}{\Delta f} \quad (2.13)$$

2.3 Modal analysis

Modal analysis is fundamental, as it enables the determination of mode shapes—illustrating how the structure deforms—and their corresponding modal frequencies. Understanding the mode shapes is crucial, as they depict the structural response to specific frequencies.

This knowledge becomes essential for identifying potential resonances and ensuring that, under normal operational conditions, the structure avoids unacceptable deformation scenarios. From a mathematical perspective, performing modal analysis requires starting from the Linear equation of motion, given as:

$$[M]\{\ddot{u}\} + [C]\{\dot{u}\} + [K]\{u\} = \{F\} \quad (2.14)$$

Here, $[M]$ is the mass matrix, $[C]$ is the damping matrix, $[K]$ is the stiffness matrix, $\{u\}$ is the displacement, $\{\dot{u}\}$ the velocity, $\{\ddot{u}\}$ the acceleration and $\{F\}$ the external forces vector. In the case of a modal analysis, the external forces are null, and it is assumed to not have damping, therefore $[C] = 0$. Assuming an harmonic motion, the displacement and acceleration are defined as:

$$\begin{aligned} \{u\} &= \{\Phi\}_i \sin(\omega_i t + \theta_i) \\ \{\ddot{u}\} &= -\omega_i^2 \{\Phi\}_i \sin(\omega_i t + \theta_i) \end{aligned} \quad (2.15)$$

Substituting these into equation 2.14, it is obtained:

$$([K] - \omega_i^2 [M])\{\Phi_i\} = \{0\} \quad (2.16)$$

This equation represents an *eigenvalue problem*, where the eigenvalues ω_i^2 are the squares of the natural frequencies and the eigenvectors Φ_i are the mode shapes. Commercial software packages usually provide efficient algorithms to compute eigenvalues and eigenvectors.

Two important parameters allow to assess the modal analysis results' correctness in software simulation environments: the mode *participation factor* and the *effective mass*.

The participation factor quantifies the extent to which a particular mode contributes to the overall motion in a specified direction or degree of freedom when the structure is subjected to dynamic loading. It provides insight into how much a specific mode is involved in the response of the structure when excited. For a given mode i , the participation factor P_i is

defined as:

$$P_i = \{\Phi_i\}^T [M] \{D\} \quad (2.17)$$

Where Φ_i is the mode shape vector for the i^{th} mode, $[M]$ is the mass matrix and D is the direction vector, which specifies the direction of interest (e.g., x, y, or z direction) for calculating the participation factor.

The effective mass in modal analysis provides a measure of how much of the total mass of a structure participates in a given mode of vibration. It is closely related to the participation factors and is an important concept for understanding the dynamic behavior of the structure. For mode i , the effective mass m_{eff_i} is defined as:

$$m_{eff_i} = \frac{P_i^2}{\{\Phi_i\}^T [M] \{\Phi_i\}} \quad (2.18)$$

This equation includes both the squared participation factor and normalization by the modal mass (term at the denominator). If the modal mass is normalized to 1 (which can be a common practice in some contexts), the effective mass simplifies to the squared participation factor.

Ideally, for each degree of freedom, the sum of the effective masses should correspond to the total mass of the body. However, this depends on how the structure is constrained, because if some of its components are fixed and can not move, they will not need to be considered in the final computation. Simulation wise, it is important to look at the ratio between the effective masses sum and the total mass, so to understand if enough modes have been extracted.

2.4 Frequency response analysis

Frequency Response Analysis (FRA) focuses on examining how a structure reacts to a particular excitation or load at a specified frequency. This analysis, conducted over a frequency range, provides a detailed portrayal of the structure's dynamic behavior within that spectrum. It is useful to analyze for example how the displacement of a structure can vary under vibrational loads with different frequencies. It is therefore strictly related to modal analysis, which predicts as well the resonance frequency of a body's components.

This type of analysis is extensively covered in Section 5.4, where the Response Power Spectral Density (RPSD) tool from ANSYS was utilized to assess the frequency distribution of displacement in the IGBT module mounting structure during its design process.

Chapter 3

Mechanical Properties and Fatigue

3.1 Mechanical Stress and Strain

To comprehensively understand the impact of vibrations on a body, it is crucial to distinguish between stress and strain. Stress denotes the external force exerted on the body due to vibrating loads, leading to deformation. The resulting deformation is referred to as strain. The interplay between stress and strain is encapsulated in stress-strain relations, also known as constitutive equations, which elucidate the material properties of the body.

Each material, especially metals, possesses an elastic limit, denoting the threshold beyond which the material undergoes plastic deformation under uni-axial stress – that is, stress applied in a single direction. Prior to surpassing the elastic limit, deformations are reversible. However, once this limit is exceeded, the deformation becomes permanent, causing the object to alter its original shape. The concept of the elastic limit is fundamental in understanding a material's response to external forces, particularly in the context of vibrations.

Furthermore, materials exhibit lower and higher yield limits under uni-axial stress. The lower yield limit signifies the point at which plastic deformation becomes noticeable. On the other hand, the higher yield limit indicates a stress level associated with more pronounced plastic deformation under uni-axial stress. Following the lower yield limit, it's essential to consider rupture stress, also known as ultimate tensile strength (UTS). Rupture stress represents the maximum stress a material can withstand under uni-axial stress before undergoing complete failure or rupture. It is the point on the stress-strain curve where the material experiences a sudden decrease in cross-sectional area, leading to failure. This characteristics are summarized in Figure 3.1.

In practical engineering applications, structures and components often experience complex multi-axial stresses rather than simple uni-axial stresses. To account for this complexity and provide a more accurate representation of material failure, the concept of von Mises stress is introduced. It was first considered by Huber in 1904 [9] and further revisited by Von Mises in 1913 [10].

Von Mises stress is a derived quantity that combines the principal stresses into a single

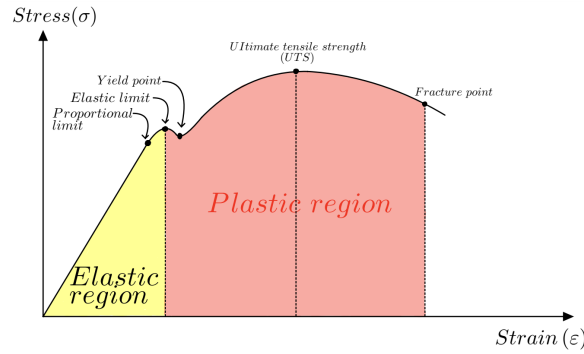


Figure 3.1: Stress strain curve

equivalent stress. It is particularly useful for predicting yielding and failure in materials under multi-axial stress conditions induced by vibrations or other dynamic loads. To better understand the Von Mises stress mathematical definition, it is necessary to know what the Cauchy stress tensor is.

The Cauchy stress tensor, named after the French mathematician Augustin-Louis Cauchy, is a mathematical concept used in continuum mechanics to describe the distribution of internal forces within a deformable body undergoing stress. It is a second-order tensor that characterizes the stress state at a specific point within a material. In a three-dimensional Cartesian coordinate system, the Cauchy stress tensor is typically represented as a 3x3 matrix. The components of the Cauchy stress tensor, denoted as σ_{ij} , describe the force per unit area acting on a surface oriented normal to the i -direction, with the force being parallel to the j -direction. The general form of the Cauchy stress tensor in a three-dimensional space is given by:

$$\begin{bmatrix} \sigma_{xx} & \sigma_{xy} & \sigma_{xz} \\ \sigma_{yx} & \sigma_{yy} & \sigma_{yz} \\ \sigma_{zx} & \sigma_{zy} & \sigma_{zz} \end{bmatrix}$$

The von Mises stress is a scalar measure derived from the Cauchy stress tensor. It simplifies the stress state information into a single value that can be compared directly to the material's yield criteria. Starting from the Cauchy stress tensor, it is calculated as:

$$\sigma_{VM} = \sqrt{\frac{1}{2} [(\sigma_{xx} - \sigma_{yy})^2 + (\sigma_{yy} - \sigma_{zz})^2 + (\sigma_{zz} - \sigma_{xx})^2 + 6(\sigma_{xy}^2 + \sigma_{yz}^2 + \sigma_{zx}^2)]} \quad (3.1)$$

Calculating the principal stresses $\sigma_1, \sigma_2, \sigma_3$ by solving the eigenvalue problem associated with the stress tensor, the following equation applies.

$$\sigma_{VM} = \sqrt{\frac{1}{2} [(\sigma_1 - \sigma_2)^2 + (\sigma_2 - \sigma_3)^2 + (\sigma_3 - \sigma_1)^2]} \quad (3.2)$$

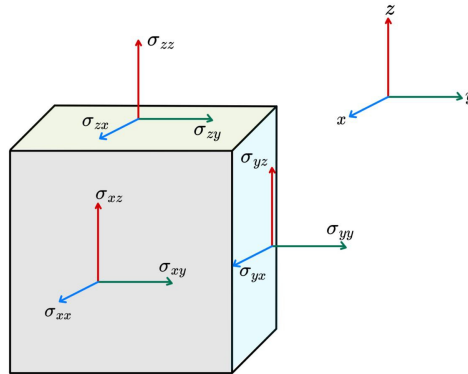


Figure 3.2: Graphical Cauchy stress tensor

The von Mises stress is particularly useful in situations where the material's yielding and failure criteria are primarily dependent on the magnitude of the stress rather than the specific orientation of the stress components. In summary, while the Cauchy stress tensor gives a comprehensive view of stress at a point, the von Mises stress simplifies this information into a single scalar quantity, facilitating the comparison of complex stress states to a material's yield criteria. The von Mises stress is the main stress value this thesis looks into, being, also in literature, one of the most important parameters regarding the reliability under vibrational loads.

3.2 Young's modulus and Poisson's ratio

Quantifying the elastic properties of a material under specific loading conditions involves two crucial parameters: Poisson's ratio and Young's modulus. Poisson's ratio serves as a measure of the Poisson effect, describing a body's deformation in the normal direction with respect to the applied loading (see Figure 3.3). On the other hand, Young's modulus pertains to the elasticity of the material.

Poisson's ratio, denoted as ν , is defined as follows:

$$\nu = -\frac{\textit{lateral strain}}{\textit{longitudinal strain}} \quad (3.3)$$

In a three-dimensional object, longitudinal strain is the change in length relative to the original length, while lateral strain measures changes in width and height, each relative to their respective original dimensions. Poisson's ratio ν typically ranges between -1 and 0.5 . A value of -1 signifies the opposite of rubber, which would exhibit high resistance to shear deformations but easy volumetric deformation (auxetic materials [11]). Conversely, a value of 0.5 indicates "volume conserving" materials. Mathematically speaking, $\nu = 0.5$ implies that

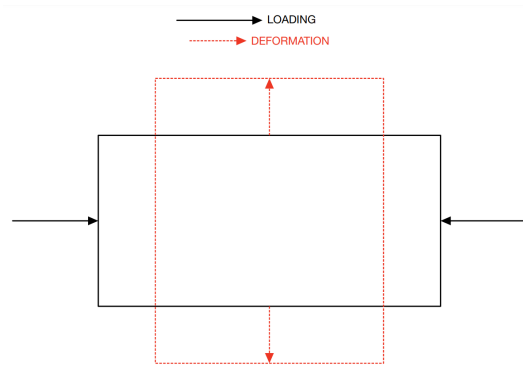


Figure 3.3: Poisson effect

the lateral strain is half in magnitude to the longitudinal strain, resulting in no net change in volume. To conserve volume, the lateral deformation, which affects two dimensions, needs indeed to be half the magnitude of the longitudinal deformation, which only affects one dimension. Materials within an IGBT module generally have a Poisson's ratios ranging between 0.2 and 0.3.

Poisson's ratio is interconnected with other material parameters, such as Young's (E), shear (G), and bulk (K) moduli. These moduli must be positive due to thermodynamic constraints [12]. While looking at Figure 3.4, the shear modulus (G) is the ratio of shear strain ($\tau = \frac{\Delta x}{l}$) to shear stress ($\gamma = \frac{F}{A}$), expressed as:

$$G = \frac{\tau}{\gamma} = \frac{F \cdot l}{A \cdot \Delta x} \quad (3.4)$$

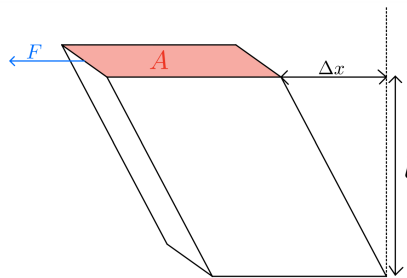


Figure 3.4: Shear modulus graphical representation

The bulk modulus is instead expressed as:

$$K = -V \frac{dP}{dV} \quad (3.5)$$

This modulus describes how a material responds to uniform pressure applied on all its faces (where P is pressure and V is volume). It's defined as the ratio of the change in pressure

to the fractional change in volume. Young's modulus is determined by the slope of the stress-strain characteristic within its elastic region. It represents the ratio of stress to the corresponding uni-axial strain during elastic deformation. All the above mentioned quantities can be expressed as function of the others starting by these three equations:

$$\begin{aligned} \nu &= \frac{3K - 2G}{6K + 2G} \\ E &= 2G(1 + \nu) \\ E &= 3K(1 - 2\nu) \end{aligned} \quad (3.6)$$

Additionally, materials can be classified as isotropic or anisotropic. In this thesis, the focus is on isotropic materials, which exhibit consistent behavior in all excitation directions.

3.3 SN Curves and Fatigue

Another crucial material property essential for estimating the expected life, particularly when deriving it from the applied stress value, is the SN curve (Stress to Number of Cycles to Failure curve). This curve establishes a relationship between the amplitude of an alternating stress and the corresponding Number of Cycles to Failure (NCF) for the examined device. Naturally, as the applied load increases, the device's capacity to withstand cycles diminishes. A typical SN curve is shown in Figure 3.5.

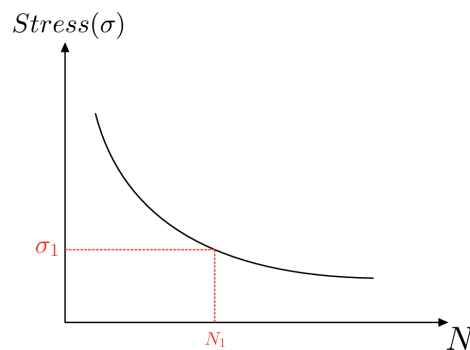


Figure 3.5: Typical SN curve

The nearly horizontal segment of the curve delineates the fatigue or endurance limit for the test material. When the applied stress amplitude remains below the endurance limit of the material, the sample is expected to have an infinite life. However, for a lot of non-ferrous metals like aluminum, a definite endurance limit may not exist. In such cases, the low-stress section of the curve does not converge into a horizontal line but rather exhibits a continuously decreasing S-N curve. In the context of random vibration analysis, the SN curve is usually

represented in two ways: the one Power law representation, often depicted in linear log-log space, and the two Power law representation, built through bi-linear curves.

- One Power Law (Linear Log-Log Space): In this representation, the SN curve is a straight line when plotted on a log-log scale. The x-axis typically represents the number of cycles (fatigue life) on a logarithmic scale, and the y-axis represents the stress amplitude, also on a logarithmic scale.
- Two Power Law (Bi-linear Curves): In this representation, the SN curve consists of two distinct linear segments on a log-log scale. The curve is divided into two regions with different slopes, indicating different fatigue behaviors at low and high stress levels. The transition point between the two linear segments is often referred to as the fatigue limit or endurance limit, representing the stress level below which the material or structure can endure an infinite number of cycles without failure.

An important parameter which highly influences the SN characteristic and therefore the expected life of components is the stress ratio. It is denoted as R and it characterizes how the load is applied. It is referred to alternating loads and is calculated as:

$$R = \frac{\text{minimum stress}}{\text{maximum stress}} \quad (3.7)$$

When the load fluctuates between positive and negative values of equal amplitude, the stress ratio is $R = -1$, indicating fully reversed loading. Conversely, if it varies only between positive (or negative) values and zero, the stress ratio is $R = 0$. For random vibrations, it can be assumed to have a totally reversible loading (i.e. $R = -1$) [13].

One common cause of failures due to random vibration is metal fatigue, which results from repeated loading. Two primary methods are used to estimate the fatigue life of structures subjected to cyclic loading: the stress life approach and the strain life approach. The stress life approach, typically used for High-Cycle Fatigue (HCF) ranging from 10,000 to 1 billion cycles, applies when stresses are below the Ultimate Tensile Strength (UTS). Conversely, the strain life approach is more suited for scenarios involving low cycle fatigue, where the cycles are fewer but the strain on the material is greater [14].

For random vibration fatigue analysis, the Steinberg formulation is the preferred method to estimate the expected life of components based on SN curves and stress levels. Originally detailed in [15], the Steinberg formulation effectively developed a robust fatigue model for predicting the lifespan of electronic components on a Printed Circuit Board (PCB) under random vibrations, with fatigue limits expressed in terms of the maximum 3σ displacement, assuming a Gaussian distribution at the natural frequency.

The Steinberg 3-band formulation incorporates the 1σ , 2σ , and 3σ stress levels. This involves considering that $P_1 = 68.27\%$ of the cycles occur at the 1σ stress, $P_2 = 27.18\%$ at the 2σ stress, and $P_3 = 4.28\%$ at the 3σ stress, as shown in Figure 3.6.

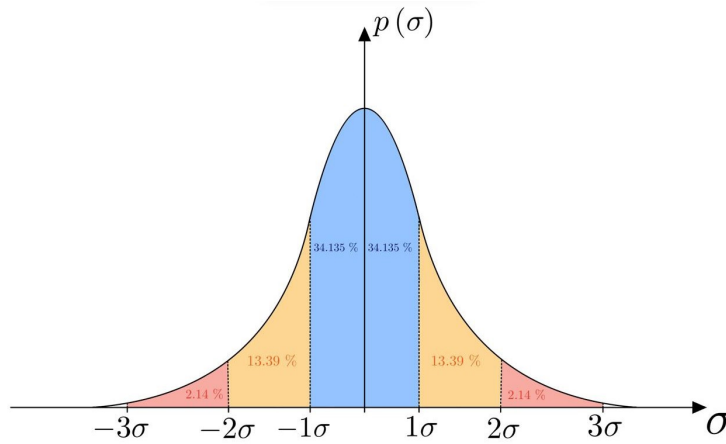


Figure 3.6: Gaussian distribution for Steinberg three band method

The utilization of the Steinberg formulation, coupled with Miner's rule, allows to calculate the total fatigue damage and the overall life expectancy of the system. Miner's rule operates on the assumption that each stress cycle depletes a portion of the structure's fatigue life. The fundamental hypothesis underlying Miner's rule says that fatigue damage is cumulative, directly proportional to the applied stress levels, and independent of the order in which the stresses are applied. This rule is expressed as:

$$D = \frac{n_{1\sigma}}{N_{1\sigma}} + \frac{n_{2\sigma}}{N_{2\sigma}} + \frac{n_{3\sigma}}{N_{3\sigma}} \quad (3.8)$$

Each term in this equation represents a fraction of the overall damage, contributing to the determination of fatigue life, which is the reciprocal of the damage. Specifically, $n_{i\sigma}$ corresponds to the actual number of cycles that have been completed by having a stress equal or below the $i\sigma$ stress level. This can be computed by starting from the statistical frequency f_0 (i.e., the number of cycles per unit time) as:

$$n_{i\sigma} = P_i f_0 t \quad (3.9)$$

Finally, $N_{i\sigma}$ corresponds to the number of cycles to failure that one can derive by looking at the SN curve considering as stress level the $i\sigma$ one.

The statistical average frequency (expected frequency in cycles per time) can be calculated by dividing the RMS velocity by the RMS displacement. This represents the number of positive zero crossings of the process per unit time, and each positive zero crossing implies one cycle of vibration [13].

When $D = 1$, we have the 100% probability that the Device Under Test (DUT) will fail. Rewriting the equation 3.8 it is obtained:

$$D = f_0 t \left(\frac{P_1}{N_{1\sigma}} + \frac{P_2}{N_{2\sigma}} + \frac{P_3}{N_{3\sigma}} \right) = n \left(\frac{0.6827}{N_{1\sigma}} + \frac{0.2718}{N_{2\sigma}} + \frac{0.0428}{N_{3\sigma}} \right) \quad (3.10)$$

Summarizing the procedure for estimating the device's lifetime expectations, what should be done is:

- Commencing with knowledge of the stress distribution and values across the three band levels.
- Utilizing the material Stress Number (SN) curve to determine the number of cycles to failure for a specific component at each of the three band levels.
- Calculating the statistical frequency.
- Computing the damage fraction for each band level.
- Summing the damage fraction terms and determining the final coefficient through Miner's rule. If it is below 1, the system is predicted not to fail.

Chapter 4

Case study

4.1 Module schematic

The subject of analysis in this thesis is the FP50R12KT4 IGBT module by Infineon [16]. Its external structure is depicted in Figure 4.1. The internal circuitry of this module is illustrated in Figure 4.2.

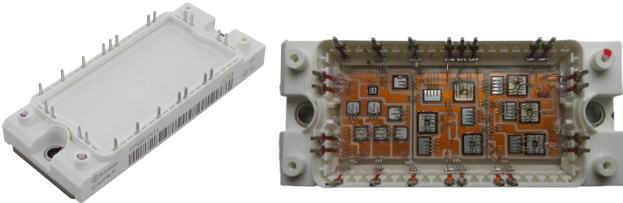


Figure 4.1: IGBT module: internal and external shape.

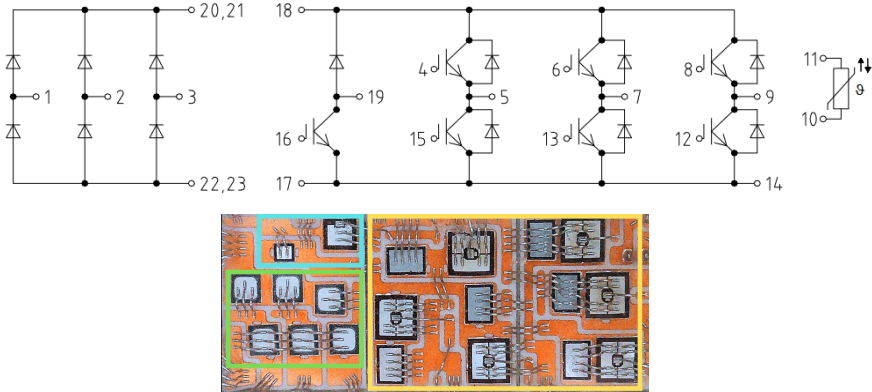


Figure 4.2: FP50R12KT4 schematic: in yellow the three phase inverter, in green the diode bridge rectifier, in blue the brake chopper

The considered IGBT module implements a three phase rectifier, a brake chopper, an inverter and an NTC (Negative Temperature Coefficient) Thermistor. The three phase rectifier, built with six diodes, simply acts as a bridge rectifier, converting three-phase AC voltage into a pulsating DC voltage. The brake chopper is useful for the fast energy dissipation required for instance to stop or control the speed of a motor. The braking technique involves converting the kinetic energy of the rotating motor into electrical energy and dissipating it as heat. The circuit does this by switching between the motor and a braking (or damping) resistor which is connected between the brake chopper's IGBT and diode. The primary of the three-phase inverter is to convert direct current (DC) into three-phase alternating current (AC) to efficiently power industrial equipment, drive large motors, and distribute electricity over long distances. Finally, the schematic shows the presence of an NTC thermistor, which is a temperature sensitive resistor used for thermal protection and monitoring. Knowing its resistance, it is possible indeed to implement safety techniques so to avoid the module to overheat.

4.2 Module Internal Structure and Materials Composition

For this thesis' purposes it is important to know the internal structure of the module. Knowing indeed its materials composition and their mechanical characteristics allows to carry out a detailed failure analysis of the device. A simplified materials stack of the IGBT module is depicted in Figure 4.3, where the layers' thicknesses are not in scale.

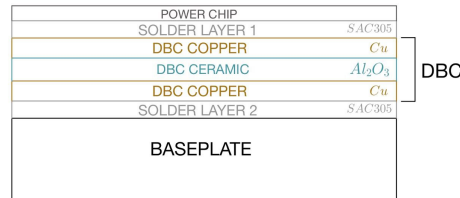


Figure 4.3: Stack of materials inside an IGBT module

The module's datasheet [16] provides a detailed material listing, indicating that the baseplate is predominantly made of copper (Cu) and includes aluminum oxide, tin, silver, among other materials in smaller quantities. This baseplate connects directly to the heatsink. A solder layer then separates this baseplate from the DBC (Direct Bonded Copper) layer, a key technology in electronic packaging that bonds copper to a ceramic substrate, usually aluminum oxide (Al₂O₃). This arrangement ensures excellent thermal conductivity and electrical insulation.

A second copper layer, depicted in orange in Figure 4.1, encapsulates the DBC structure, and another layer of solder precedes the placement of the silicon chip to enhance its attachment. Atop the silicon, aluminum pads host the Aluminum bond wires, soldered directly onto them.

Analyzing the material composition is crucial for assessing the reliability of IGBT modules under vibration. Materials' distinct mechanical properties mean that they respond differently to mechanical stresses induced by vibrations, potentially leading to failures through various mechanisms. Hereafter is reported table which summarizes all the most important characteristics of the materials.

Material	ρ [$\text{kg} \cdot \text{m}^{-3}$]	Young's modulus (GPa)	Poisson's ratio	SN curve
Aluminum	2710	70 [3],[17]	0.33 [3],[17]	Section 4.3
Aluminum oxide	4000	400 [18]	0.23 [18]	[19]
Silicon	2330	130 [20]	0.28 [21]	[22],[23]
Copper	8960	120 [24]	0.33 [25]	[26]
SAC305	7380	26.2 [27],[28],[17]	0.42 [28]	[29]

Table 4.1: Materials' properties summary.

4.3 Bond wires' SN curve

This section is particularly important, given that the aluminum bond wires are the most susceptible to stress. As explained further in the following chapters and as outlined in the literature review of this thesis, there exists a considerable risk of encountering cracks at the near the foot of these bond wires. Consequently, it is imperative to precisely characterize their mechanical properties.

The formulation of the SN curve originates from the analysis presented in [30]. The primary objective of this study was to empirically determine the Stress to Number of Cycles to Failure curve for diverse stress ratios, followed by modeling the results to establish a comprehensive model applicable across varying R ratios. Their investigation initiated with the derivation of stress-strain characteristics, from which the tensile strengths for bond wires with diameters of $300 \mu\text{m}$ and $500 \mu\text{m}$ were deduced. Given that the IGBT module under consideration specifies bond wire diameters less than or equal to $400 \mu\text{m}$, the analysis focused on the $300 \mu\text{m}$ case. Once they derived the SN characteristics for R ratios spanning from 0.1 to 0.7, the results were fitted through a linear and a non linear method, using the equations in 4.1.

$$\begin{aligned}
 \text{linear} \quad \log(\sigma_a) &= a_L + b_L \cdot \log(N) \\
 \text{nonlinear} \quad \log(N) &= a_{NL} - b_{NL} \cdot \log\left(\frac{\sigma_a - c_{NL}}{\sigma_{aTS} - \sigma_a}\right)
 \end{aligned} \tag{4.1}$$

In these equations:

- σ_a refers to the alternating stress, that corresponds to $\sigma_a = \sigma_{max} - \sigma_{avg}$
- σ_{aTS} refers to the transformation of the tensile stress into a stress amplitude, which also depends on the stress ratio based on the formula $\sigma_{aTS} = \sigma_{TS} \cdot \frac{1-R}{2}$
- N refers to the number of cycles to failure
- a , b and c refer to the fitting parameters

Once completed the fitting, they were able to derive the equations showing the dependence of the fitting parameters on the R ratio. Particularly, they confirmed that the non linear method proves valuable also in determining the fitting parameters also outside the considered 0.1 to 0.7 stress ratio range. Therefore, the equations which have been also used in this thesis, where the stress ratio for random vibrations has been taken as $R = -1$ ([13]) are reported in Equation 4.2.

$$\begin{aligned} a_{NL} &= 0.996 \cdot R + 5.114 \\ b_{NL} &= -0.869 \cdot R + 3.125 \\ c_{NL} &= -16.237 \cdot R + 15.913 \end{aligned} \quad (4.2)$$

Finally, after imposing $R = -1$, the resulting SN curve has been plotted and is depicted in Figure 4.4. Moreover, Table 4.1 summarizes all the materials' main properties discussed in this chapter.

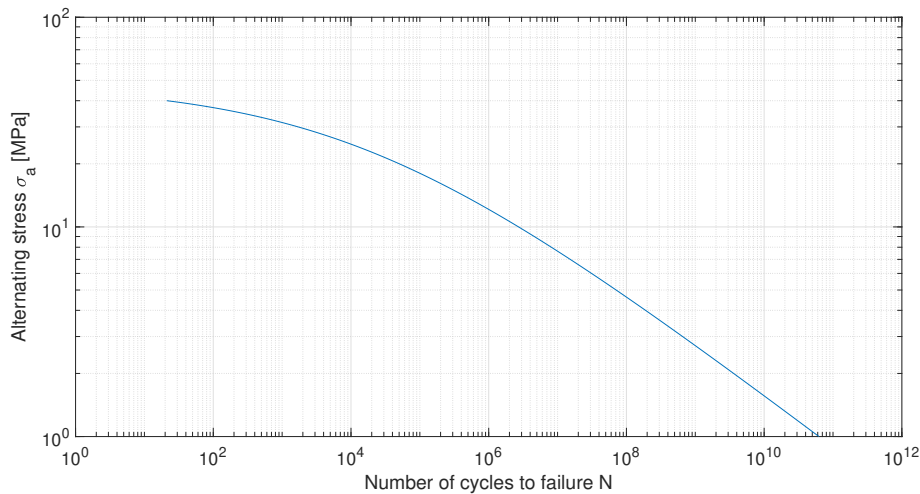


Figure 4.4: SN curve for aluminum in log log scale

4.4 Inverter bare dies

The inverter IGBT bare die utilized in this IGBT module is the Low Power Chip IGC50T120T8RL from Infineon [31]. Its shape is reported in Figure 4.5.



Figure 4.5: IGBT bare die: real and theoretical shape.

The IGBT bare die comprises four different Aluminum zones on top of the black Silicon zone. One is the gate contact, one is the test contact (to not be used) and the remaining two are the emitter pads. The architecture used in this IGBT is the Trench gate field-stop (TGFS) one. The main difference of this IGBT structure is the addition of a Field Stop n- layer. This layer introduces two major improvements. Firstly, the FS layer helps to create a more uniform electric field throughout the chip. This allows the chip to withstand a higher voltage before electrical breakdown occurs. Moreover, it reduces the time it takes for electrical charges to recombine. This leads to better overall performance when the chip is switching states. The inverter diodes utilized for the three phase inverter are fast switching emitter controlled diodes (IDC28D120T8M from Infineon [32]). The datasheet and real bare die shape can be seen in Figure 4.6.



Figure 4.6: Diode bare die: real and theoretical shape.

4.5 Dimensions and thicknesses summary

In table 4.2 are reported all the thicknesses and dimensions of each layer.

	Component	Thickness [μm]	Width [mm]	Length [mm]
Aluminum pad	Inverter IGBTs	3.2	5.4	5.74
	Inverter diodes	3.2	5.346	3.526
	Brake chopper IGBT	3.2	4	4
	Brake chopper diode	3.2	2.026	2.326
	Rectifier diodes	8	3.5	3.5
Silicon layer	Inverter IGBTs	111.8	6.84	7.25
	Inverter diodes	106.8	4.5	6.3
	Brake chopper IGBT	111.8	4.99	5.45
	Brake chopper diode	106.8	2.98	3.3
	Rectifier diodes	302	4.8	4.8
Solder layer 1	Inverter IGBTs	85	6.84	7.25
	Inverter diodes	85	4.5	6.3
	Brake chopper IGBT	85	4.99	5.45
	Brake chopper diode	85	2.98	3.3
	Rectifier diodes	85	4.8	4.8
Copper DBC 1	-	300	27.8	23
Ceramic layer	-	380	29	24
Copper DBC 2	-	300	27.8	23
Solder layer 2	-	250	27.8	23
Baseplate	-	3000	38	107.5

Table 4.2: Thicknesses and dimensions of each layer for a simplified IGBT module model

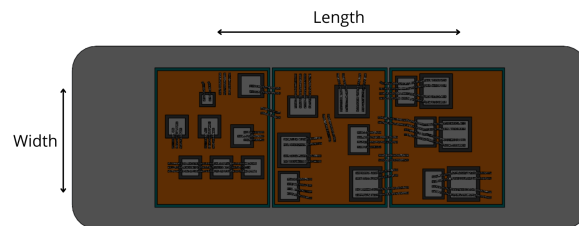


Figure 4.7: Simplified top view of the IGBT model

4.6 Final module model

The IGBT module was accurately modeled in 3D using various software tools. The structural components were designed using SolidWorks, while the bond wires were modeled in Rhinoceros 3D due to SolidWorks' limitations in handling such detailed features. Rhinoceros is particularly suitable at creating bond wires thanks to the MFis Wire tool, which not only ensures consistent contact surface shapes for each wedge bond wire connection but also allows for adjustable height and radius, ensuring a perfectly defined model without design inaccuracies. For simplicity, the bond wires were categorized into four groups: left, central, right, and terminal. These were subsequently assembled using SolidWorks. The complete assembly was then exported as an IGES file, which was imported into ANSYS for simulation purposes. The final model of the IGBT module is illustrated in Figure 4.8.

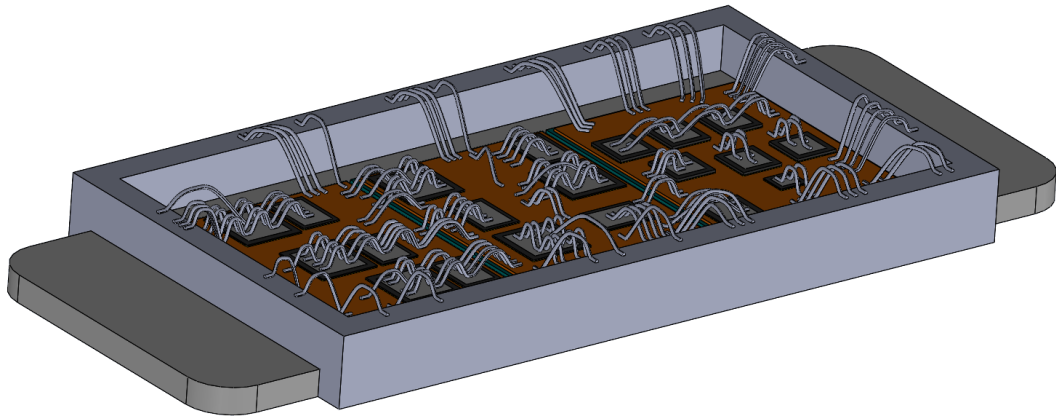


Figure 4.8: Final IGBT module 3D model

Chapter 5

Vibration simulation in ANSYS

5.1 Modal analysis

To conduct a random vibration analysis in ANSYS Multiphysics, it is essential to first perform a modal analysis in order to obtain results through a mode superposition method. Similarly, for harmonic analysis, although it can also be solved using a "full" (i.e., non-approximated) method, the same procedure is required. The environment that has been used for this thesis is ANSYS Mechanical.

When conducting a modal analysis in ANSYS, it is crucial to accurately define all structural characteristics. This allows the simulator to precisely extract resonance frequencies and their corresponding mode shapes. One of the most critical characteristics to define is the support, which can vary in types. For the simulations undertaken in this thesis, the "fixed support" has been selected as the most suitable option. Specifically, for the structure and type of vibration being analyzed, the system can be compared to a building with its base fixed to the ground, experiencing an earthquake. The boundary condition "fixed support" refers to the base of the building, which, being anchored to the ground, does not need to be considered in the modal analysis, as it does not experience a motion relative to ground.

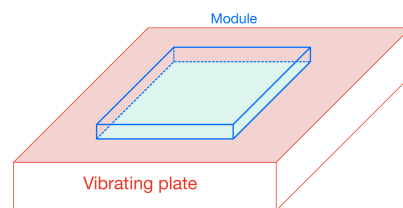


Figure 5.1: Simplified structural illustration

As is depicted in Figure 5.1, the IGBT module will be mounted on top of a vibrating plate (see chapter 6). The light blue area refers to the *fixed support*, that is indeed fixed to the plate. Once the plate is vibrating, it is fundamental to derive how the module "free-

to-move" components will deform. The closer the vibrating frequency is to the resonance frequencies of the module, the higher the displacement and the stress will be.

In addition to selecting the fixed support, it is crucial to determine the number of modes to extract. Typically, it is recommended to extract modes up to at least the resonance frequency equal to 1.5 times the maximum vibration frequency, as a general guideline. However, in the case of the IGBT module under consideration, numerous bond wires with varying shapes are present on the module, resulting in different frequencies for their respective modes. Given the presence of tens of bond wires and the necessity for precise results, it is considered appropriate to extract not only the first or second mode of each bond wire during simulations. Therefore, as a compromise between computational constraints and accuracy, 100 modes have been extracted.

5.2 Harmonic and Random Vibration environments

Harmonic analysis can be conducted using either a mode superposition method or a full harmonic method. The former involves a linear combination of mode shapes to determine the displacement vector of the structure. The solver computes the response of the structure across a range of frequencies, which can be selected with a specified number of points. ANSYS calculates the response for each point, yielding three possible outcomes: frequency response, phase response, and contour plots. Frequency response provides values across a frequency range, while phase response indicates the phase lag between input and output. Contour plots depict the distribution of strains, stresses, etc., at specific frequencies.

The full harmonic method is more accurate but computationally expensive. It eliminates errors that may occur because of modal truncation and is typically employed for systems with high damping, where complex mode shapes make responses difficult to obtain correctly through linear mode superposition.

In the context of this thesis, the full harmonic method is not required, as the results obtained through mode superposition are precise enough.

Regarding instead Random vibration analysis, in ANSYS, users have the ability to insert one of four types of Power Spectral Density (PSD) curves as input excitation for structures: displacement, velocity, g acceleration, and $\frac{mm}{s^2}$ acceleration. The quality of the PSD input curve is crucial for achieving accurate results, and ANSYS aids this process by visually displaying the PSD curve in color. A curve is considered to have good fidelity if the increase in Power Spectral Density between consecutive frequency points does not exceed one order of magnitude.

Furthermore, the selection of boundary conditions is a critical input parameter that determines the surfaces where excitation will be applied. In the context of this thesis "fixed support" is used as the random vibration boundary condition, serving as the source of the excitation. Looking at the random vibration analysis results, ANSYS allows to extract the 1σ , 2σ , or 3σ values, which offer insights into the maximum potential deformation or stress occurrence with corresponding probabilities.

Calculating derived quantities such as principal stresses, stress intensity, and equivalent stress is challenging due to the non-Gaussian nature of their probability density functions. This non-Gaussian distribution of the derived quantities and in particular of the Von Mises stress is analyzed in [33], which offers an histogram showing the usual probability function of such derived quantity.

To handle these complexities, ANSYS Mechanical utilizes the Segalman-Fulcher algorithm, an advanced method that improves the traditional single degree of freedom (DOF) method. The single-DOF response analysis, which simplifies structural complexity by focusing on a specific mode of vibration or deformation, is considered overly simplistic for assessing the global response of a system to random vibrations. The Segalman-Fulcher algorithm [34] enables a more comprehensive evaluation by considering all excited modes and frequencies of interest. It facilitates the calculation of the Root Mean Square (RMS) Von Mises stress at a node using a formula derived through the modal superposition method.

ANSYS provides also the Response PSD tool (RPSD), which, upon selecting a point, reveals its spectrum response under random excitation. This tool illustrates potential resonance points and the distribution of power across different frequencies. The RMS value, equivalent to a 1σ value in statistical terms, is obtained by taking the square root of the area under the PSD. Analyzing the centroid of the area under the PSD curve and its corresponding frequency (i.e., the expected frequency) can offer insights into whether the output power of the response aligns with or is close to the natural frequency.

Animations of vibrations are not available in random vibration environment simulations, as their results are derived just through mathematical methods. Conversely, the harmonic analysis environment allows for the visualization of animations showing how vibrations excite the structure. Therefore, to validate the setup of random vibration simulations, they have been compared with harmonic analysis by examining the resulting stresses and displacements in a simplified 3D model of the module under identical vibration conditions. This comparison involved choosing specific accelerations and frequencies applied in both scenarios. For random vibrations, the Power Spectral Density (PSD) spectrum was limited to a one-Hertz bandwidth centered around the target frequency. The method hereafter explained was used to determine the necessary PSD amplitude for input.

The acceleration PSD is measured in $\left[\frac{g_{RMS}^2}{Hz}\right]$. Thus, within a single Hertz bandwidth, the PSD amplitude should correspond to the square of the selected RMS g acceleration value used in the harmonic analysis. Therefore, upon selecting an acceleration, its RMS value, given its sinusoidal behavior in harmonic analysis, was computed by dividing by the square root of two. Subsequently, this value was squared to obtain g_{RMS}^2 , which was then used as input PSD value. Equation 5.1 summarizes this simple process.

$$\int_{f_1}^{f_2} PSD df = a_{RMS}^2 [g_{RMS}^2] \Rightarrow PSD = \frac{a_{RMS}^2 [g_{RMS}^2]}{\Delta f [Hz]} = \frac{a_{RMS}^2}{1} \left[\frac{g_{RMS}^2}{Hz} \right] = \frac{a^2}{2} \left[\frac{g_{RMS}^2}{Hz} \right] \quad (5.1)$$

The resulting shape of the random vibration PSD curve is illustrated in Figure 5.2.

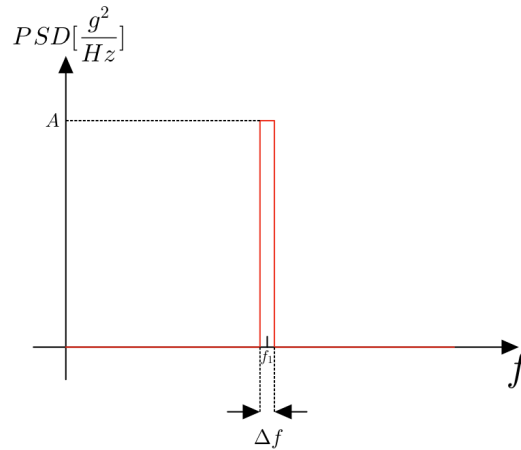


Figure 5.2: Random vibration PSD curve for harmonic analysis comparison

After inputting identical vibrating conditions into both environments' simulations, there was the need to compare results such as displacements and Von Mises stresses. As previously discussed, harmonic analysis yields deterministic results, whereas random vibration analysis provides statistical expectations on them. Specifically, the outputs of random vibration analysis are presented as 1σ , 2σ , and 3σ values. However, in this context, randomness is nearly eliminated, and also the random vibration consists only of a deterministic sinusoidal signal at a single frequency.

When comparing the harmonic vibration with the 1σ , 2σ , and 3σ values obtained from random vibration analysis, an approximation can be made. Assuming the amplitude A of the deterministic sinusoidal vibration remains constant throughout the analysis, the 1σ value of the random vibration can be considered as an estimate of the RMS (Root Mean Square) amplitude of the deterministic sinusoidal vibration. Hence, the 1σ value derived from random vibration analysis can be approximated as $\frac{A}{\sqrt{2}}$, representing the RMS amplitude of the deterministic sinusoidal vibration.

In simulation environment, four different levels of acceleration (a) were tested for validation purposes: 20 g, 30 g, 40 g, and 50 g. Finally, the maximum stresses have been identified for different frequencies and the harmonic ones have been divided by $\sqrt{2}$ to be compared with the 1σ values of the random vibration. In both harmonic and random vibration environment, the excitation was applied at the bottom surface of the module model reported in Figure 4.8, following the inputs reported in Table 5.1.

The plots for the four acceleration levels are reported in Figure 5.3. Just the stresses on the most stressed bond wire are reported, as to comply with meshing limitations while still keeping a good accuracy.

As is shown, the harmonic and random analysis resulting stresses are identical, since the trajectories are perfectly overlapped. This demonstrates the correctness of the random vibration excitation.

Harmonic analysis acceleration	Random vibration PSD $\frac{g_{RMS}^2}{Hz}$ value
20 g	$200 \frac{g_{RMS}^2}{Hz}$
30 g	$450 \frac{g_{RMS}^2}{Hz}$
40 g	$800 \frac{g_{RMS}^2}{Hz}$
50 g	$1250 \frac{g_{RMS}^2}{Hz}$

Table 5.1: Acceleration values for each number of plates, to keep a constant area under the peaks

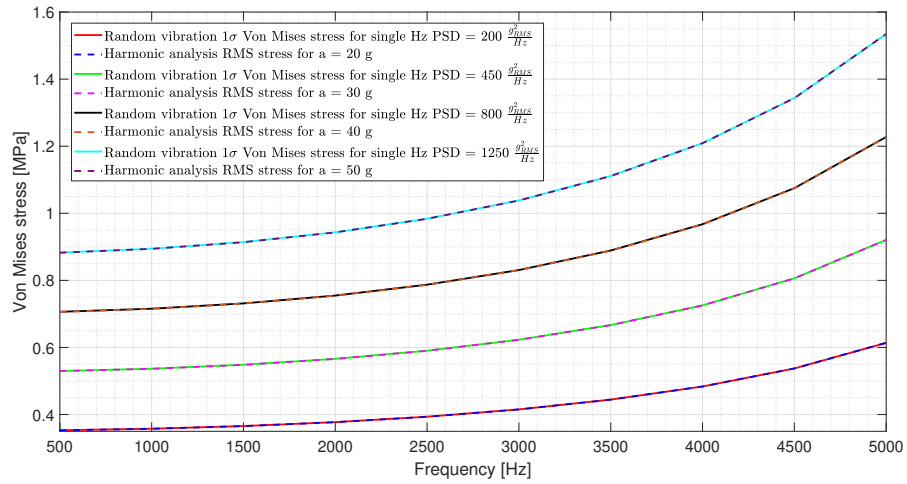


Figure 5.3: Comparison between harmonic and single Hz random excitation stresses.

5.3 Fatigue in ANSYS

ANSYS provides support for fatigue analysis in the frequency domain, specifically for random vibration and harmonic analysis. It employs the stress life method, where the fatigue life is determined by the relationship between stress (S) and the number of cycles to failure (N). The SN curve, illustrating this relationship, is typically characterized by discrete data points and can be expressed by a One Power Law or a Two Power law relationship. If the linear or bi-linear SN curve is not directly defined, the ANSYS mechanical fatigue tool linearly interpolates just the starting and ending discrete point values through the following equation:

$$NS^m = A \quad (5.2)$$

Where N is the number of cycles to failure, S is the stress amplitude in [Pa], m is the fatigue strength exponent and A is the fatigue strength coefficient. In ANSYS engineering data, there is the possibility to define SN curves by specifying parameters such as A and m . For a

bi-linear representation, it's a matter of adding a section with distinct fatigue stress exponent (r) and coefficient (C) [14].

Counting the number of cycles to failure is vital for assessing the lifespan of a device within random vibration environments, a task made complex by their statistical nature. ANSYS offers three cycle counting methods for random vibration fatigue: Narrow-bandwidth, Steinberg, and Wirsching formulations. The Narrow-bandwidth method, specific for narrow frequency ranges, and the Wirsching method, aligned with oil and gas industry standards, are unsuitable for the broader and more general applications addressed in this thesis. Consequently, these methods are not employed here. Instead, the Steinberg formulation is used. This formulation is favored due to its versatility and applicability to a wide range of industries and vibration scenarios.

5.4 Resonator design and testing

ANSYS proved practical in the design and testing phase of what has been called *resonator*. Designing it was primarily fundamental as it acted as a structure to properly install the IGBT module over the vibrating surface of the machinery which will be described in the next chapter. Directly mounting the module directly on top of the vibrating plate proved indeed impossible due to differences in the mounting hole distances. Additionally, as the machinery only generated six degrees of freedom random vibration, deriving the expected life dependence on factors such as excitation frequency or displacement solely using a basic aluminum plate as an adapter was challenging. Thus, the solution involved designing a mounting structure to function as a mechanical filter. This structure aimed to selectively excite certain frequencies over others, thereby approximating the random vibration of the vibrating table as a simple harmonic vibration. Consequently, both random and harmonic vibration environments could be analyzed using the same equipment, simplifying experimental testing. The design process started with the drawing in SolidWorks of two basic aluminum plates: one intended for attachment to the vibrating plate and the other serving as a mounting platform for the IGBT module. The manner in which these plates were interconnected dictated the structure's capability to selectively stimulate certain frequencies over others.

The primary criteria that the resonator needed to verify were, firstly, its robustness to withstand the vibrating environment it was designed for without breaking. Secondly, for better comparison between simulation and experimental results, it needed to exhibit only the first and second mode shapes (translational) within the 10-5000 Hz bandwidth. This ensured that primarily two out of the six degrees of freedom were stimulated, facilitating comparison with harmonic analysis with excitation along specific axes. Lastly, the resonator needed to accommodate the stacking of additional plates, allowing for the adjustment of mass on top of it. Consequently, like in a mass-spring system, this facilitated the variation of the excited frequency, enabling analysis of the module's expected life under different operating frequencies. The final design of the resonator is shown in Figure B.4.

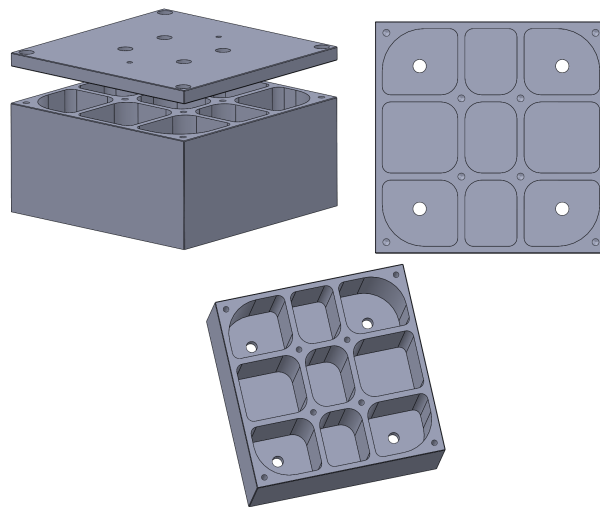


Figure 5.4: Final resonator design

In the image just one stack plate is shown, but many more can be stacked. The height of the resonator base is equal to 8 mm, while every one of its walls is 0.5 mm thick. The resonator was then tested in ANSYS to validate its functionality. Initially, a modal analysis was performed to ensure that only the first two modes fell within the 10-5000 Hz bandwidth, as mentioned earlier. Subsequently, a parallelepiped with an equivalent total weight to the IGBT module (179.5 g) was placed on top of the resonator, and the excitation at the module's base was characterized. Figure 5.5 depicts the first three modal shapes of the resonator, while their respective resonance frequencies versus the number of stacked plates are reported in Figure 5.6.

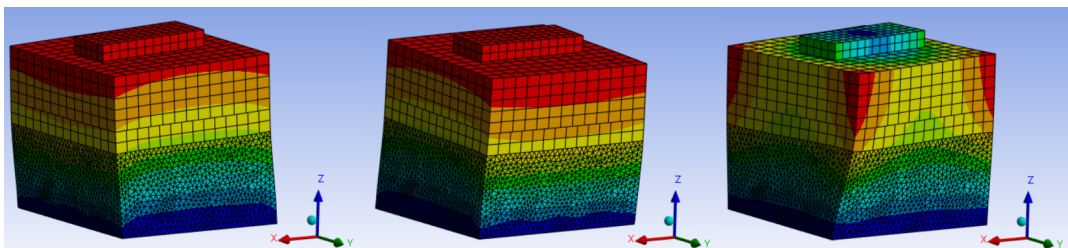


Figure 5.5: First, second and third modal shapes

As observed, the first two resonance frequencies decrease appropriately with an increase in the number of stacked plates or, equivalently, with an increase in the weight placed on top of the resonator. It was decided to limit the stacking to a maximum of seven plates. Beyond this limit, the final structure would have become excessively large without substantial additional contributions to the frequency range. Since the resonance frequencies of the bond wires are far from the chosen 2 kHz limit, there was little justification for examining frequen-

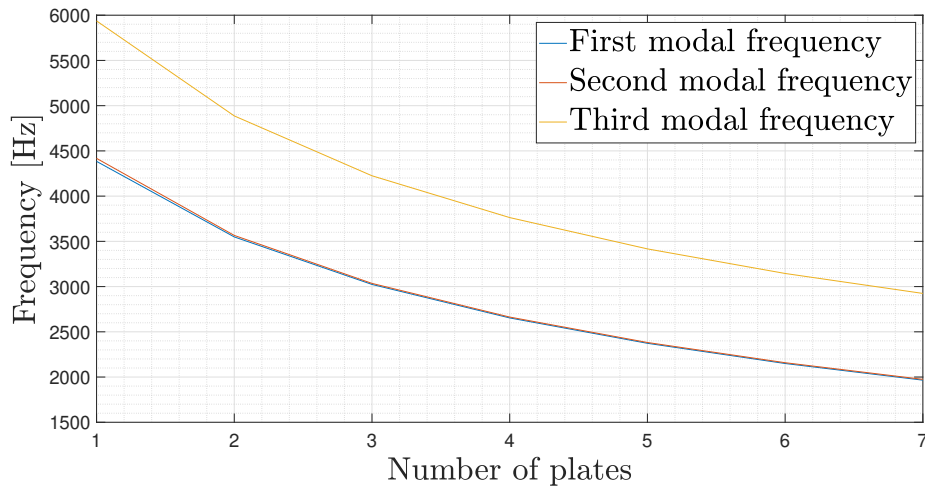


Figure 5.6: First and second modal frequencies vs number of stacked plates

cies around 1 kHz, as the resulting stresses would likely be comparable to those observed at 2 kHz.

In the plot, the third modal frequency has also been included, which corresponds to a torsional mode shape. This mode could potentially be excited, considering that the vibrating plate possesses six degrees of freedom. However, it has minimal impact on the expected lifespan of the bond wires because it does not cause significant translational displacement, which in turn would lead to substantial oscillation of the free end of the bond wire.

To validate the performance of the resonator, a tri-axial random vibration was applied at its bottom surface and the displacement response PSD on its top surface (where the module is mounted) was extracted. The response PSD (Power Spectral Density) refers to the distribution of power over frequency components in a signal. ANSYS offers a graphical representation showing how the power of the response (displacement in this case) varies with frequency. This information allows to identify frequencies where the displacement is significant, which correspond to frequencies where the resonator is actually amplifying the vibration.

Below are the plots displaying the displacement response PSDs for varying numbers of plates. In each of the seven cases, the acceleration PSD value has been maintained constant at $0.5 \frac{g_{RMS}^2}{Hz}$ across the bandwidth ranging from 10 to 5000 Hz.

The plot demonstrates the effective functionality of the resonator, obtaining vibration excitation at various frequencies by adjusting the number of plates. Comparing the seven trajectories with the one without the resonator, it's visible that vibration characteristics remain largely similar outside the amplified ranges. The linear decrease in the line is a result of constant acceleration across the frequency spectrum, with higher displacements corresponding to lower frequencies.

Although the resonator is functioning correctly, its primary objective lies in comparing

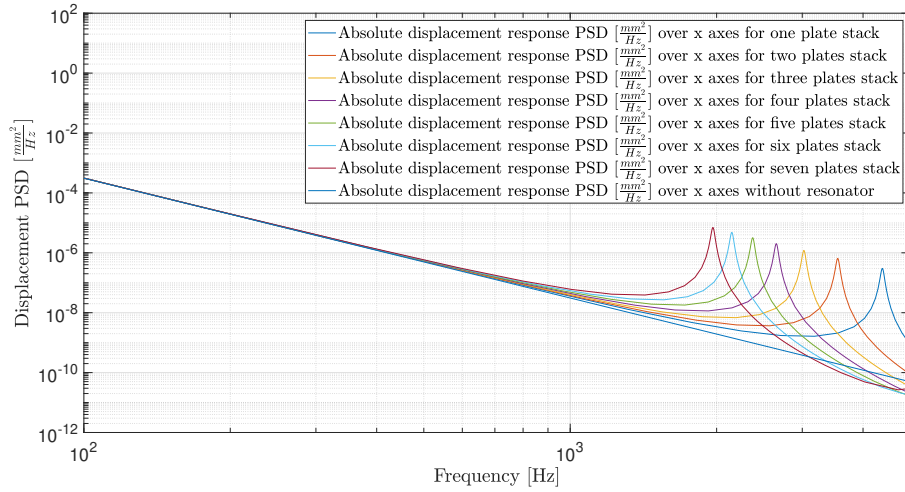


Figure 5.7: Absolute displacement RPSDs comparison with constant acceleration values

stress variations with operating frequency. Hence, despite the higher displacements observed in the lower frequency range, they are expected to have a negligible impact on the overall lifespan. If the acceleration PSD value was maintained constant regardless of the number of plates, as shown in Figure 5.7, the displacements would vary each time. Ensuring that displacement remains constant is essential for directly correlating stresses with frequency. This necessitates guaranteeing that the areas under each peak are equal. By assuming that stresses depend solely from these peaks, maintaining equal areas enables each area to be associated with an equivalent harmonic analysis displacement, ensuring consistency across frequencies.

To achieve this goal, the proposed testing approach involves reducing the total acceleration g_{RMS} value as the number of plates increases, thereby counteracting the effect of the increasing response PSD values. To correctly calculate the areas, the peaks were integrated over frequency with MATLAB. Initially, the focus was on calculating the areas under the curves for the X-axis displacement RPSDs, in order to adjust the acceleration values. Subsequently, these adjusted acceleration values were utilized to check if also the areas under the Y-axis displacement RPSD curves remained constant. After the acceleration levels equalization, the resulting trajectories are shown in Figure 5.8, while the equalized acceleration levels are reported in Table 5.2.

As a final step, it was crucial to calculate the equivalent displacement for each resonator configuration to ensure it remained constant. The first step in computing the displacement values for the equivalent harmonic vibration involved considering the areas under the peaks, which had been previously calculated using MATLAB. As anticipated, the areas exhibit nearly identical values for every number of stacked plates, approximately $A = 2.81 \cdot 10^{-5} \text{ mm}^2$. By taking the square root of the area, the RMS (Root Mean Square) value of displacement is derived, which serves as an appropriate input value for the harmonic analysis.

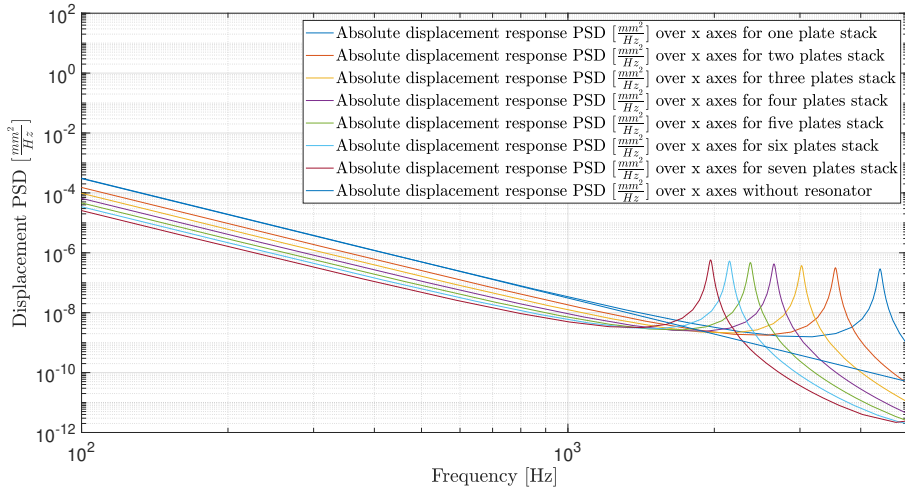


Figure 5.8: Absolute displacement RPSDs comparison with the same peaks' areas

Number of plates	PSD $\frac{g_{RMS}^2}{Hz}$ value	Acceleration g_{RMS} value
1	0.480	48.94
2	0.243	34.82
3	0.155	27.81
4	0.105	22.89
5	0.074	19.22
6	0.055	16.57
7	0.041	14.30

Table 5.2: Acceleration values for each number of plates, to keep a constant area under the peaks

The obtained value is equal to $5.31 \mu\text{m}$. More in detail, Table 5.7 offers both the calculated displacements and peak frequencies of the equivalent harmonic analyses along the X and Y axis.

5.5 Modal analysis results

As mentioned earlier, modal analysis serves as a crucial step in characterizing stress distribution across the IGBT module, and therefore allows the derivation of an expected life model. Indeed, the stress amplifies near the foot of a bond wire when the excitation frequency closely aligns with its resonance frequency.

Initially, a modal analysis was carried out using ANSYS for each bond wire. This analysis involved fixing supports on every horizontal face expected to interface with the copper or

Num. of plates	f_{peak} [Hz]	d [μm]
1	4383	5.33
2	3548.1	5.31
3	3022.9	5.31
4	2652.8	5.31
5	2372.3	5.29
6	2149	5.34
7	1964.9	5.33

Table 5.3: X axes equivalent displacements

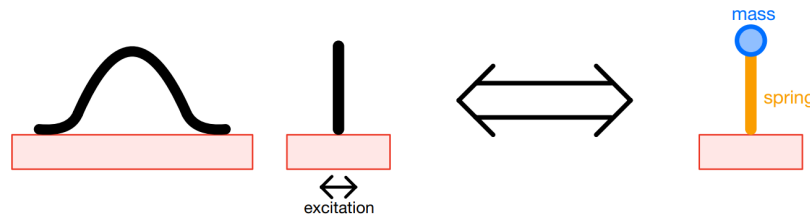
Num. of plates	f_{peak} [Hz]	d [μm]
1	4416.2	5.28
2	3564.7	5.27
3	3034.4	5.29
4	2662	5.21
5	2381.3	5.31
6	2157.9	5.37
7	1973.9	5.36

Table 5.4: Y axes equivalent displacements**Table 5.5:** Summary of the equivalent harmonic analyses parameters.

aluminum layer. Subsequently, the results were validated through mathematical derivation, resulting in a formula capable of predicting the first resonance frequency of a bond wire based on its main characteristics.

Given that the student version of ANSYS permits solving a maximum of 128,000 nodes and elements, and considering the necessity for a finely meshed analysis to accurately assess bond wire characteristics, the modal analysis was carried out singularly on each bond wire, so to use the minimum possible body sizing, which was selected equal to 0.055 mm. A mathematical validation of the resulting modal frequencies has been done as well.

To do that, each bond wire has been approximated as a mass-spring system, as depicted in Figure 5.9.

**Figure 5.9:** Three main shapes for terminal bond wires

Furthermore, the wire has been considered as a thin and homogeneous beam subjected to transverse excitation (i.e., perpendicular to the direction of the tensile force). The equations have been derived using Euler-Bernoulli theory, which characterizes the response of thin and flexible beams under loads.

In particular, for a mass spring system it is known that the resonance frequency, without damping, is given by:

$$f_n = \frac{1}{2\pi} \sqrt{\frac{K_{wire}}{m_{wire}}} \quad (5.3)$$

where f_n is the wire n^{th} resonance frequency [Hz], K_{wire} is the wire rigidity [$\frac{N}{m}$] and m_{wire} is the wire mass [kg].

Although determining the mass of the wire is straightforward using its volume and density, calculating its rigidity is more complex. The formula for rigidity has been derived by utilizing the findings from [35]. Thus, the rigidity of the wire is expressed as:

$$K_{wire} = \frac{C_w E_w I_w}{l_{eff}^3} \quad (5.4)$$

where C_w is a wire shape dependent parameter, E_w is the wire Young's modulus [Pa], I_w is the second moment of inertia of the bond wire [m^4] and l_{eff} is the wire effective length [m].

The second moment of inertia, also called area moment of inertia, is a measure of an object's resistance to bending or flexural deformation. It quantifies how the mass is distributed around a given axis. Mathematically, it is defined as the integral of the squared distance from each infinitesimal element of mass to the axis of interest, summed over all the mass elements:

$$I_w = \int r^2 dm \quad (5.5)$$

where r is the distance from the axis of interest to the mass element and dm is the mass of the infinitesimal element. Solving the integral for a thin wire with circular area, it is obtained (as in [36]):

$$I_w = \frac{\pi r^4}{4} \quad (5.6)$$

The effective length of the wire is taken as half of the total wire length, given the approximation depicted in 5.9.

By inserting all the parameters into equation 5.3, it is obtained:

$$f_n = \frac{1}{2\pi} \sqrt{\frac{2 \cdot C_w E_w r^2}{l^4 \rho}} \quad (5.7)$$

Depending on the value of n and the specific shape of each wire, the parameter C_w will vary accordingly, making it impractical to assume uniformity across all bond wires. However, as an initial reference point, the C_w value obtained for the first resonance frequency in [35] has been adjusted to align with the parameters used in this thesis. While in [35], an elastic modulus of $E_w = 69$ GPa and an aluminum density of $\rho = 2700 \frac{kg}{m^3}$ were employed, in this thesis, $E_w = 70$ GPa and $\rho = 2710 \frac{kg}{m^3}$ were utilized. The adapted shape coefficient for the first resonance frequency resulted being therefore $C_w = 50.72$. With this value, the calculated resonance frequencies were quite lower than the simulated ones. Therefore, after

an adaptation of the shape parameter to the shape of the bond wires of the IGBT module analyzed here, the resulting fitting parameters were: 78 for the terminal bond wires and 91.5 for the other ones. The necessity for adaptation is justified by the fact that, while in [35] the bond wires' lengths for 2.5 mm high bond wires were around 25 mm, here the lengths are around 10 mm. The shape is therefore completely different.

Table 5.6 summarizes the simulated modal frequencies with their correspondent modal shapes for some of the bond wires (the ones which will be analyzed more in detail also in the next sections), offering also a comparison with the calculated ones.

As can be seen from the table, the formula is useful for estimating the first resonance frequency of a given bond wire, aiding in understanding which vibrations are likely to cause damage and potentially lead to its rupture.

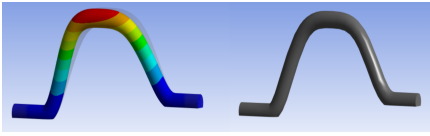
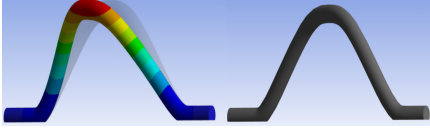
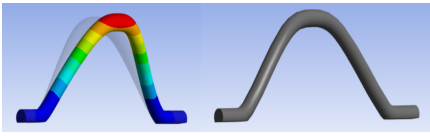
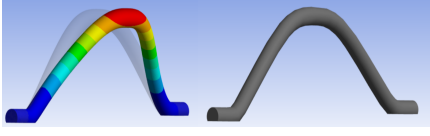
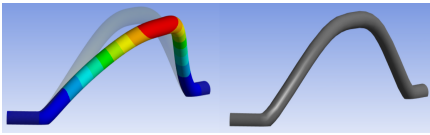
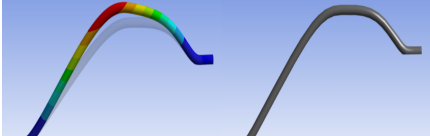
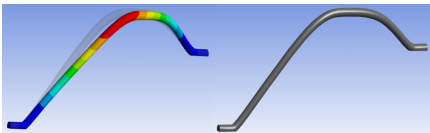
bond wire	Length	Simulated f_1	Calculated f_1
	7.960 mm	34.593 kHz	34.533 kHz
	9.640 mm	23036 kHz	23.551 kHz
	10.018 mm	21.318 kHz	21.805 kHz
	11.265 mm	17.310 kHz	17.244 kHz
	12.178 mm	15.679 kHz	14.756 kHz
	14.734 mm	9.354 kHz	9.306 kHz
	16.265 mm	7.642 kHz	7.637 kHz

Table 5.6: Summary table for bond wires modal frequencies

5.6 Harmonic and Random Vibration results

During the resonator characterization, it was assumed that only the peaks were responsible for generating stress in the bond wires during random vibration operation with the resonator. The displacements corresponding to equivalent harmonic vibrations centered at the resonator's resonance frequencies were derived and are shown in Table 5.7.

In the harmonic analysis conducted using ANSYS, the displacement was kept constant at $5.31 \mu\text{m}$, and the stresses on the bond wires were extracted for each of the seven resonance frequencies. This procedure aimed to compare the stress dependency on frequency from the harmonic analysis with that obtained using the resonator under random acceleration. By observing whether the stress patterns were similar, it could be determined if the resonator effectively allowed for the determination of stress frequency dependence.

An important consideration regarding harmonic analysis must be made. While the harmonic excitation was applied along a single axis only, random vibration was tri-axial. Therefore, it was necessary to assume that stresses on certain bonds were caused solely by excitations along the y axis, while on others solely from the x axis, as depicted in Figure 5.10.

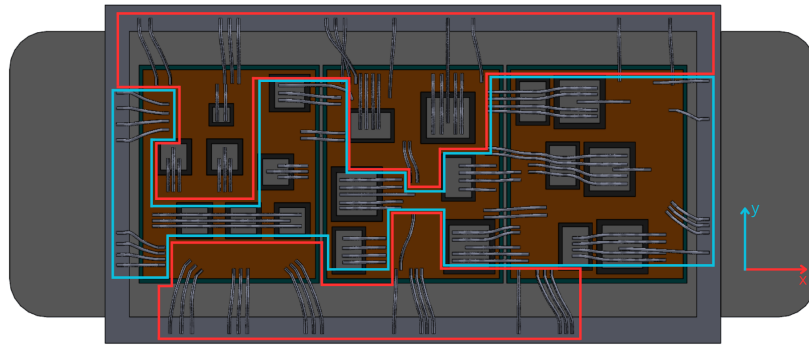


Figure 5.10: Stress dependence on the excitation directions.

In Figure 5.10, the bond wires highlighted in blue have been assumed to have stresses only caused by y axis excitations, and vice-versa, the ones in red to have stresses only caused by x axis excitations. This approach allowed for applying harmonic excitation along a single axis and comparing its results with tri-axial random vibration. Simulation results confirmed that for bond wires aligned along the x axis, the stress is predominantly due to the y axis, and vice versa.

In the random vibration setup, the simulation setup involved mounting the IGBT module 3D module on top of the resonator and stimulating the resonator's bottom surface through the PSD (Power Spectral Density) acceleration values obtained from Table 5.2. The random vibration was tri-axial (i.e., along, x, y and z directions).

In Figure 5.11 are shown the structures used to derive the final simulation results. The system utilized to carry out the random vibration analysis coincides perfectly with the one which has been mounted over the vibrating surface in the experimental work. For simplicity, in Figure 5.11 only the resonator with two stacked plates is depicted, but the results are reported more generally for one to seven stacked plates.

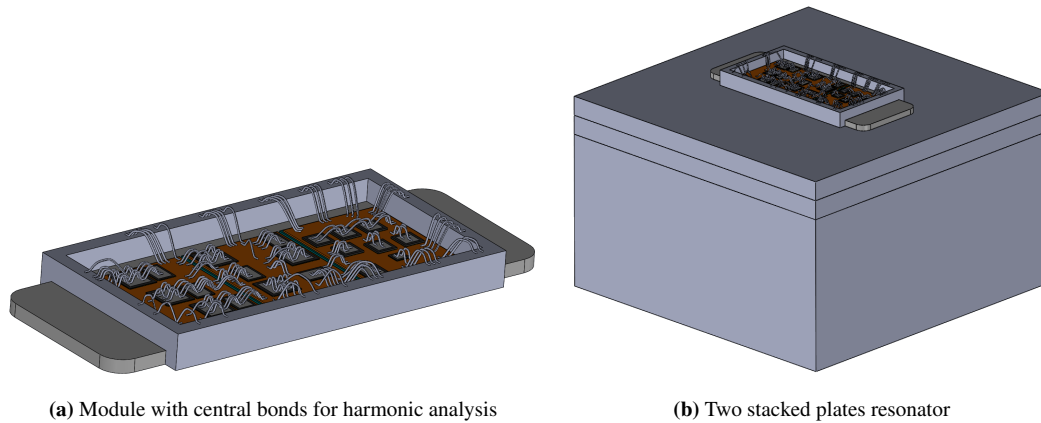


Figure 5.11: Harmonic and random vibration used structures.

Using the structures provided, the following procedure was adopted to compare the results of harmonic and random analysis.

Initially, by selectively suppressing some groups of bond wires, the most stressed bond wire was identified for both harmonic and random vibration analysis. As anticipated, the location of maximum stresses was the same in both scenarios, occurring near the feet of the longest bond wires in each group. Being the longest implies having the lowest first resonance frequency.

Subsequently, after identifying the most stressed bond wire, a finer mesh was employed to better simulate that bond wire behaviour. The goal was to maintain uniform mesh body sizing for both harmonic and random analysis across all inputs, ensuring highly accurate results. For this purpose, the larger structure, specifically the resonator with 7 stacked plates, was considered, and only the longer bond wire was left unsuppressed. It was established that using a mesh body sizing of 0.07 mm for a single bond wire helped keep the number of nodes in the FEA below 128,000, facilitating subsequent analyses. Additionally, the number of modes to be extracted was set at 100, deemed sufficient to analyze the most relevant modes.

Based on these decisions, 49 separate simulations were conducted for the random analysis using the resonator: for each of the 7 resonator configurations, and for each of the four bond wire groups (i.e., left region chip-level bonds, central region chip-level bonds, right region chip-level bonds, terminal bonds), the most stressed bond wire aligned on the X-axis and the most stressed bond wire aligned on the Y-axis were tested using a mesh body sizing of 0.07 mm. Hence, for each resonator configuration, 7 bond wires were tested independently (since one of the groups had bond wires aligned only along the X-axis). This method

derived the maximum stresses for each group and each resonator configuration.

The same process was then replicated in the harmonic analysis, where only 7 simulations were needed, as ANSYS allows for frequency range sweeping and extraction of results at specific frequencies of interest.

Ultimately, all results were compiled and illustrated in Figures 5.12, 5.13, 5.14 and 5.15 which display the dependence of maximum stresses on frequency for the four groups of bond wires in both harmonic and random analysis.

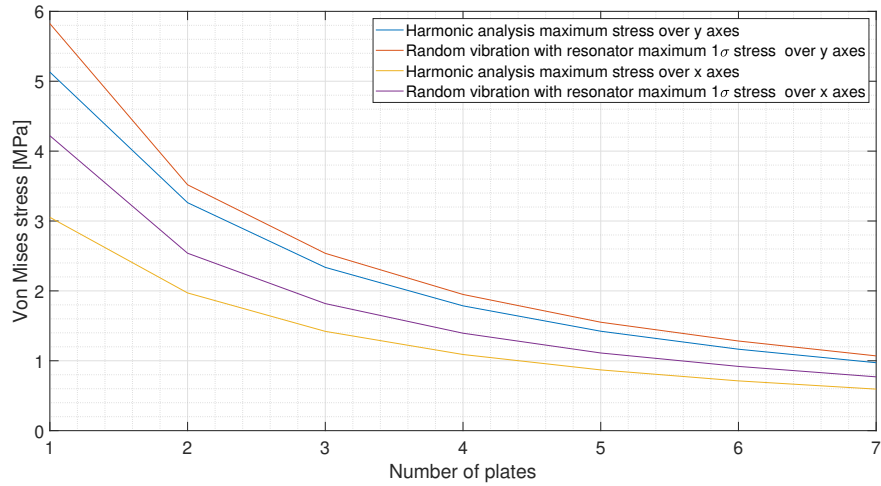


Figure 5.12: Central region chip-level bonds stresses comparison.

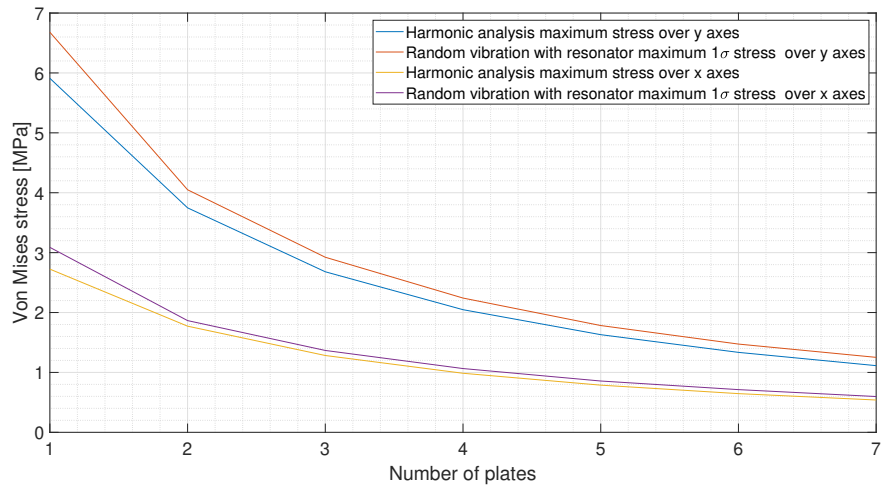


Figure 5.13: Left region chip-level bonds stresses comparison.

Several observations can be made regarding this plots. Firstly, it's evident that for both

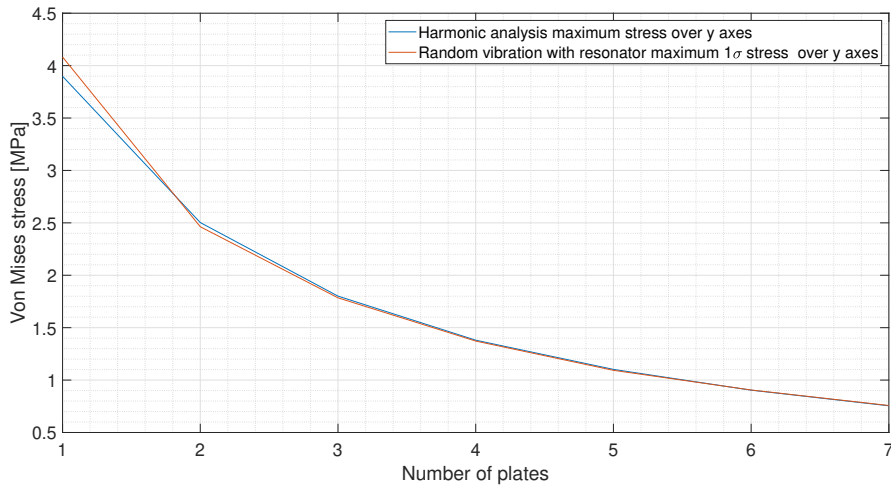


Figure 5.14: Right region chip-level bonds stresses comparison.

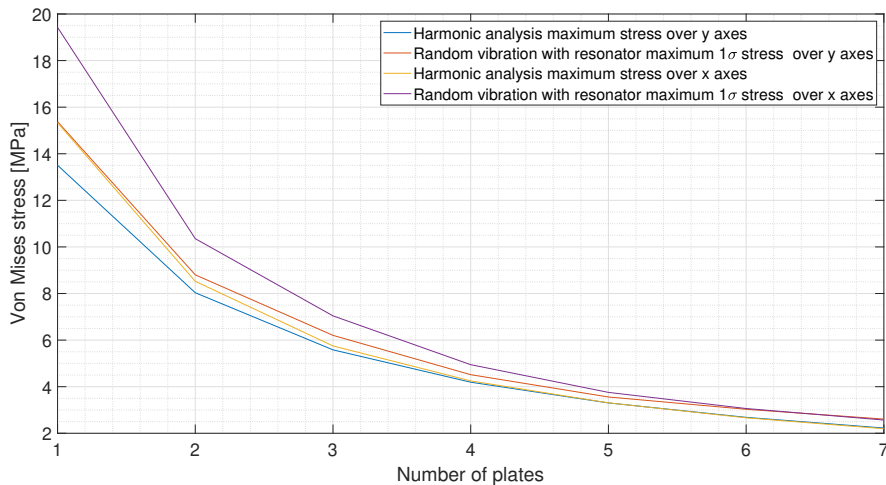


Figure 5.15: Terminal bonds stresses comparison.

the x and y axis excitation directions, the stresses induced by random vibration are slightly higher than those from harmonic analysis. This outcome was expected because random vibration covers a wide frequency spectrum, thereby including frequencies near and beyond those considered in the harmonic analysis, which in turn focuses just on the peak energy. Consequently, the random analysis resulting stress incorporates the effects of nearby frequencies, contributing to the overall higher stress levels.

Furthermore, it is notable that the stress behavior remains consistent between both the harmonic and random vibration scenarios with the resonator. This validation aligns with expectations, indicating that the resonator effectively approximates random vibration as a

harmonic analysis. Consequently, this approach enables the extraction of stress dependencies on excitation frequency.

Moreover, the stress distribution shown in the plot for the terminal bond wires indicates that these experience particularly significant stress due to their lower first resonance frequency compared to other bond wires. Consequently, it is apparent that the first modal frequency is a critical parameter in this study. This frequency is directly influenced by the bond wire length and thickness, suggesting that longer and thinner bond wires are more susceptible to higher stress levels and, thus, have a greater likelihood of failure. Therefore, to ensure the safety of the bond wires under any vibration conditions to which the module may be subjected, it is crucial to prevent the operational frequency of the module from nearing the first modal frequencies of the bond wires.

5.7 Simulated expected life

The simulated expected life has been derived for the longest terminal bond wire, which is the most stressed one and should be the first failing inside the module. Its life expectancy is reported in a log log scale in Figure 5.16 with respect to the resonator resonance frequency.

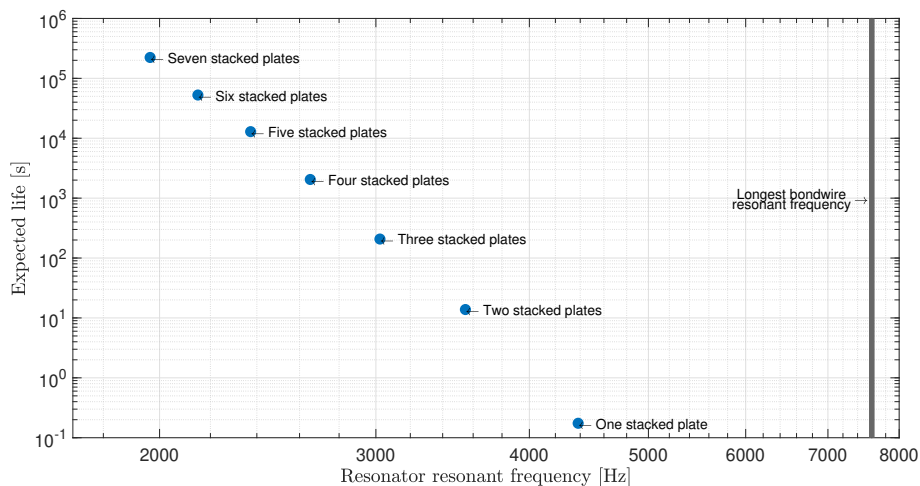


Figure 5.16: Simulated expected life: the blue dots represent the expected life of the longest bond wire; the grey line shows where the first resonance frequency of the longest bond wire is.

The plot shows with blue dots the life expectancy for each number of stacked plates, while adopting the previously mentioned equalized accelerations. It also shows with a grey vertical line the lowest bond wire resonance frequency (i.e., the one correspondent to the longest terminal bond wire). It can be seen how, after a correct calibration, the resonator has been designed so that it should cause the instant failure of the terminal bond wire while it has just one stacked plate. However, decreasing the peak frequency and reaching the lowest

peak frequency at around 2 kHz, it can be seen how the terminal bond wire should be able to sustain continuous vibrations for around 10^5 seconds, which correspond to about 28 hours.

In addition to understanding the Expected Life of a component, it's crucial to comprehend its 1σ Von Mises stress distribution as well. This distribution indicates where failures are more likely to occur. Two images are included below, displaying contour plots for both the stress distribution and the Expected Life of the most stressed terminal bond wire and the most stressed chip-level bond wire.

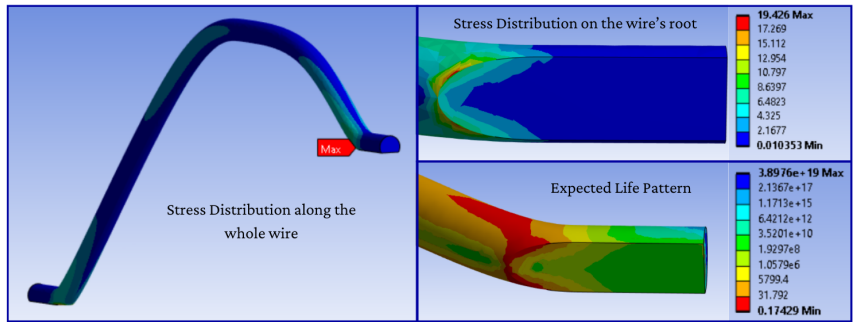


Figure 5.17: Contour plots of the 1σ Von Mises stress [MPa] and Expected Life [s] for the most stressed terminal bond wire.

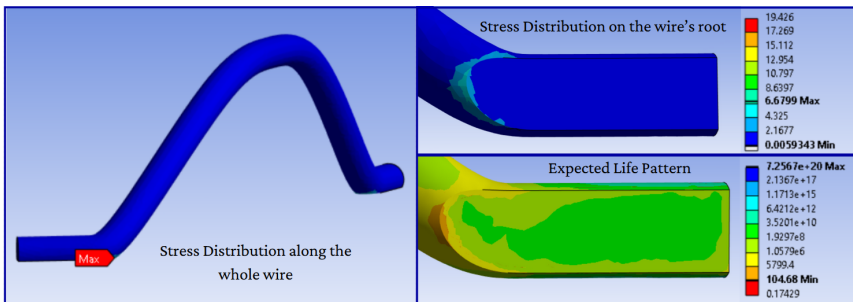


Figure 5.18: Contour plots of the 1σ Von Mises stress [MPa] and Expected Life [s] for the most stressed chip-level bond wire.

As anticipated from the literature review, the stress concentration near the foot of the bond wire is evident. This results in an Expected Life pattern that underscores the likelihood of observing cracks along the red areas. Furthermore, these contour plots hold true for all other bond wires as well, even if with lower stresses due to their varied dimensions.

A clear difference is visible between the Expected Life contour plots in Figure 5.17 and 5.18. The most stressed chip-level bond wire experiences significantly lower stress than the most stressed terminal bond wire, making it much less likely to fail first.

Finally, it is important to note that the simulations predict the terminal bond wires are more likely to fail near the points where they connect to the external module pins, rather than near the foots where they connect to the module PCB.

Number of plates	f_{peak} [Hz]	Random Acceleration g_{RMS}	d [μm]
1	4383	49	5.33
2	3548.1	35	5.31
3	3022.9	28	5.31
4	2652.8	23	5.31
5	2372.3	19	5.29
6	2149	17	5.34
7	1964.9	14	5.33

Table 5.7: Resonator configurations: peak frequencies, equalized acceleration input levels and equivalent harmonic analysis displacements.

Chapter 6

Experimental campaign

6.1 Equipment description

This section provides a description of the equipment used in the experimental setup, which entirely revolves around the functionalities of the Espec Qualmark Typhoon 2.5 HALT chamber. It is a state-of-the-art environmental testing chamber designed for accelerated stress testing. This chamber is capable of simulating a wide range of environmental conditions, including rapid temperature changes and vibration testing. It was chosen for its versatility and precision, ensuring that the experimental conditions could be tightly controlled and varied according to the requirements of the study. In addition to the Typhoon 2.5, other instruments and tools were employed to monitor the experimental data, ensuring accuracy and reliability in our results. These supplementary tools will be described in the following sections.

The most important feature of the Typhoon 2.5 is its vibrating surface. It includes a total of 64 threaded holes, each with a 3/8-inch diameter and a 16 threads per inch (TPI) pitch. The holes are arranged in a grid pattern, with the center of each hole positioned 4 inches away from the center of its neighboring holes, both horizontally and vertically. The table size proves well-suited for Highly Accelerated Life Testing (HALT) applications and various Highly Accelerated Stress Screening (HASS) applications. Its main feature is to have a Six Degree of Freedom (6DOF) Vibration characteristic. This includes translational movements along the X, Y, and Z axes, as well as rotational movements in pitch, roll, and yaw (see Figure 6.1). The capability to simulate vibrations in multiple directions allows for a more comprehensive and realistic simulation of real-world conditions.

Another key feature of this vibrating plate is its ability to generate Random Excitations. The term "Random" implies that the vibration signals are unpredictable and non-repetitive, mirroring the varying nature of real-world vibrations. PSD, or Power Spectral Density, is a crucial aspect of managing vibrations. It characterizes the distribution of power across different frequencies in a random vibration signal. The Vibration Range of the system is specified to be from 5 to 75 g_{RMS} (root mean square acceleration) across frequencies ranging from 10 Hz to 5000 Hz. This information provides details on both the amplitude (in g_{RMS})

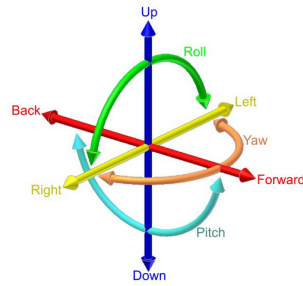


Figure 6.1: Six Degrees of Freedom motion [37].

and the frequency range of vibrations that the system can generate.

The Typhoon 2.5 control software allows users to input the desired g_{RMS} value, regulating the acceleration through a PID controller connected to an accelerometer mounted in the vertical direction. While this g_{RMS} value inherently accounts for movements in other directions, it primarily corresponds to the vertical direction. The functioning block scheme is reported in Figure 6.2.

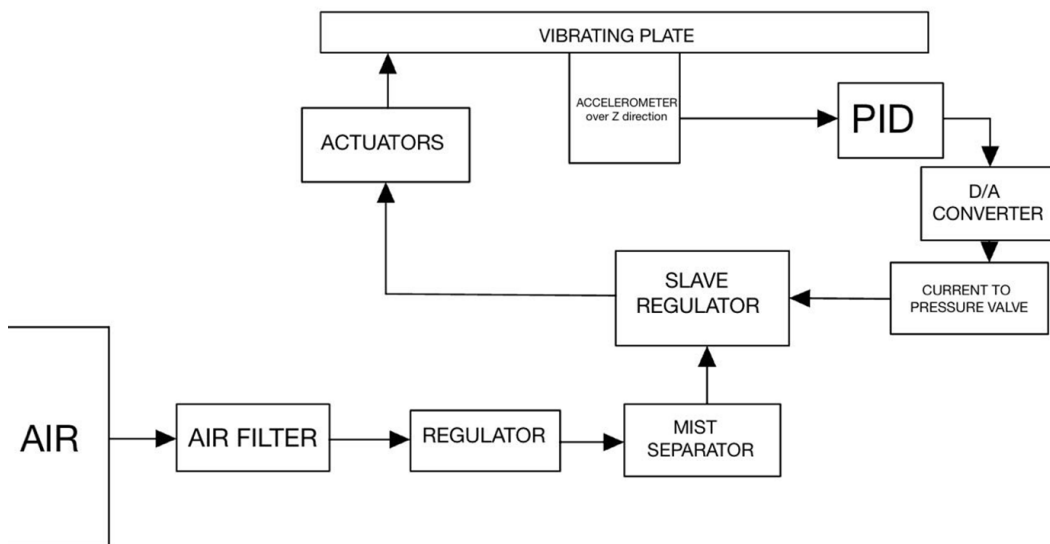


Figure 6.2: Vibrating plate control block scheme

The machine effectively manages the PSD to ensure that specifications are maintained throughout testing. Assuming a constant PSD over the specified frequency range and simplifying to a single degree of freedom, the PSD can be calculated from the g_{RMS} value of the vertical direction vibration using the formula:

$$PSD \left[\frac{g^2}{Hz} \right] = \frac{g_{RMS}^2}{\Delta f} \quad (6.1)$$

This formula reflects the relationship between the g_{RMS} value and the frequency bandwidth (Δf), providing a simplified yet effective way to calculate the Power Spectral Density.

Screenshots of the control panel and chamber setup of the Typhoon 2.5 are provided in Appendix A. In the control panel screenshots, the key values to note are the *Vibration Setpoint*, representing the user-defined vibration acceleration level, and the *Table Control Vib.* value, which indicates the actual reading from the accelerometer. After clicking the *Chamber On/Off* button, users can set any desired vibration level. In the chamber setup screenshots, users can configure all the PID parameters to adjust how quickly the system reaches the desired setpoint. Additionally, safety limits for vibration levels can be set in *Vibration High Limit (Grms)* and *Vibration Backup Limit (Grms)*. Exceeding these limits triggers an alarm and shuts down the chamber. An Ethernet connection was established to enable communication between the chamber and the control computer.

6.2 Module mounting structure

As introduced in the previous chapter, a resonator was designed and then produced. All the structure is built in Aluminum. The final real resonator is shown in Figure 6.3, where both the resonator base and the structure with one stacked plate are displayed. A more comprehensive image is reported in Appendix B, where a bigger view is depicted.

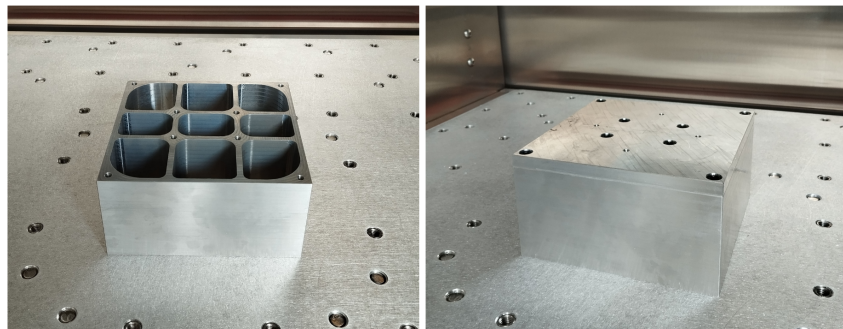


Figure 6.3: Real resonator

6.3 Monitoring circuit

To evaluate the integrity of the module, a circuit was designed featuring an Arduino DUE board, BJTs, resistors, and LEDs. Based on the schematic of the IGBT module, this setup was particularly necessary for testing the integrity of all the bond wires as well as the components. The Arduino board was chosen for its ease of handling the activation and deactivation patterns of the IGBTs and diodes. To illustrate how the circuit operates, a simplified schematic is provided in Figure 6.4. The schematic does not include the gate drivers, which

will be explained later on. Moreover, it highlights the monitoring components with thinner lines for clarity.

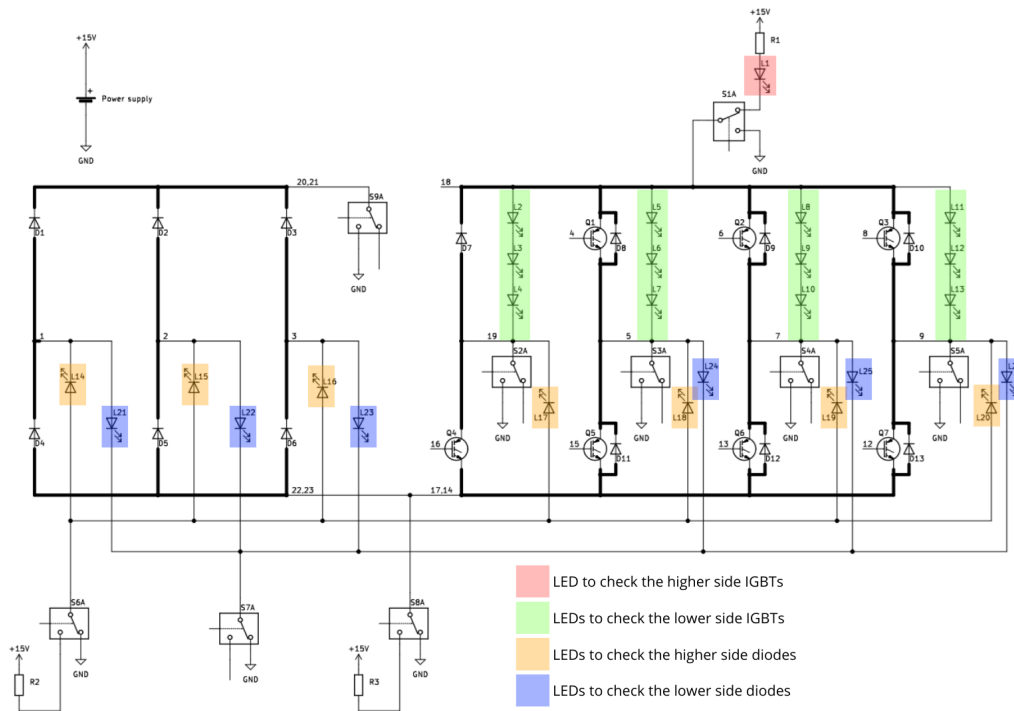


Figure 6.4: Simplified schematic for continuity measurement: thicker connections refer to the IGBT module original schematic

To effectively monitor all components in the circuit and identify potential failures, a systematic approach is implemented. Initially, each IGBT is biased individually in a specific sequence (Q1, Q2, Q3, Q4, Q5, Q6, Q7), while ensuring the diodes remain off. Subsequently, two distinct groups of diodes are activated. By observing the behavior of the LEDs during these stages, any abnormalities indicative of failure can be identified. To better describe the circuit’s operational sequence and its capacity to assess module integrity, here is reported a table, which contains the state of each component depending on the pattern the system is in, and also the state of each one of the selectors indicated in the schematic as S1A - S9A.

To highlight the circuit functionalities two examples are here reported, one for a pattern where one IGBT is turned on (e.g., Pattern 1), and one for a pattern in which a group of diodes is turned on (e.g., Pattern 8). The equivalent circuit in Pattern 1 is visible in Figure 6.5, while the one in Pattern 8 in Figure 6.6.

During Pattern 1, when IGBT Q1 is activated, the voltage across pin 18 and pins 19, 5, 7, and 9 matches the ON voltage drop of the IGBT. Assuming proper functionality of both the IGBT and the bond wires linking terminals 18 (collector signal Q1), 4 (gate signal Q1), and 5 (emitter signal Q1), the LEDs in all branches (L2-L4, L5-L7, L8-L10, L11-L13)

Component	Pt.1	Pt.2	Pt.3	Pt.4	Pt.5	Pt.6	Pt.7	Pt.8	Pt.9
Q1	ON	OFF	OFF	OFF	OFF	OFF	OFF	OFF	OFF
Q2	OFF	ON	OFF	OFF	OFF	OFF	OFF	OFF	OFF
Q3	OFF	OFF	ON	OFF	OFF	OFF	OFF	OFF	OFF
Q4	OFF	OFF	OFF	ON	OFF	OFF	OFF	OFF	OFF
Q5	OFF	OFF	OFF	OFF	ON	OFF	OFF	OFF	OFF
Q6	OFF	OFF	OFF	OFF	OFF	ON	OFF	OFF	OFF
Q7	OFF	OFF	OFF	OFF	OFF	OFF	ON	OFF	OFF
D1-D3 + D7-D10	OFF	OFF	OFF	OFF	OFF	OFF	OFF	ON	OFF
D4-D6 + D11-D13	OFF	OFF	OFF	OFF	OFF	OFF	OFF	OFF	ON
S1A	15 V	15 V	15 V	15 V	15 V	15 V	15 V	GND	GND
S2A	GND	GND	GND	O.C.	O.C.	O.C.	O.C.	O.C.	O.C.
S3A	GND	GND	GND	O.C.	O.C.	O.C.	O.C.	O.C.	O.C.
S4A	GND	GND	GND	O.C.	O.C.	O.C.	O.C.	O.C.	O.C.
S5A	GND	GND	GND	O.C.	O.C.	O.C.	O.C.	O.C.	O.C.
S6A	GND	GND	GND	GND	GND	GND	GND	15 V	GND
S7A	GND	GND	GND	O.C.	O.C.	O.C.	O.C.	O.C.	GND
S8A	GND	GND	GND	GND	GND	GND	GND	GND	15 V
S9A	GND	GND	GND	GND	GND	GND	GND	GND	O.C.

Table 6.1: States of each component in the circuit's patterns

remain OFF since their activation voltage exceeds that of the IGBT. Conversely, LED L1 is ON to indicate the integrity of the signal-carrying bond wires. If an IGBT failure occurs, the four series LED branches illuminate due to the higher voltage. Alternatively, if a bond wire failure results in an open circuit, L1 switches OFF. This behavior persists across Patterns 2 and 3. Patterns 4-7 follow a similar logic with inverted states: when, for example, Q4 is active, L1-L2-L3-L4 illuminate under normal conditions, but all LEDs are turned OFF in the event of a failure. This configuration enables straightforward monitoring of IGBTs and bond wire integrity through distinctive LED patterns from Pattern 1 to Pattern 7.

During Pattern 8, when all the IGBTs are deactivated, the system's power supply is reversed and directed towards the anodes of LEDs L14-L20. Under normal conditions, current flows through these LEDs, subsequently activating D1-D2-D3-D7-D8-D9-D10. Conversely, LEDs L21-L26 remain OFF due to open-circuited cathodes. Any failure in a diode or in a bond wire results in the corresponding LED in its branch switching OFF. Pattern 9 follows a similar principle, but with voltage applied to the anodes of diodes D4-D5-D6-D11-D12-

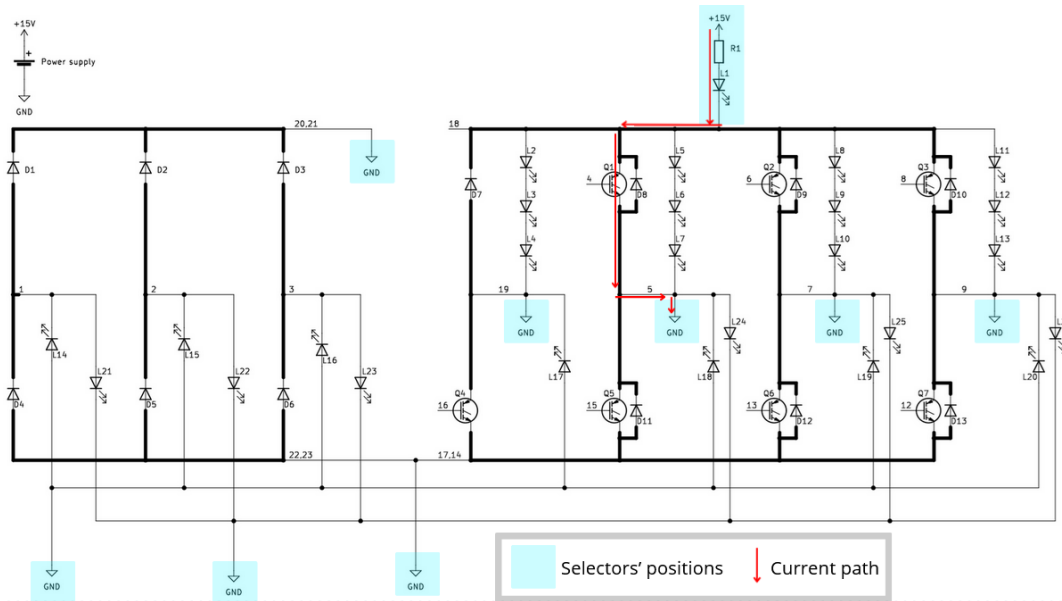


Figure 6.5: Simplified schematic for Pattern 1: LED L1 and IGBT Q1 are turned on.

D13. Consequently, current flows through LEDs L21-L26. Once again, any bond wire or diode failure causes the associated LED to remain OFF, facilitating fault detection.

Up to now, it has not been discussed how the IGBT are turned ON and OFF and how the selectors are realized. Here comes the importance of using the Arduino board, which allows a simple yet effective approach to address this problem. Since Arduino can not output from its digital ports more than 5 V, there was the need of using a buffer (BJT BC547B), which could allow a connection to the 15 V power supply. A simplified schematic of the switch implementation is shown in Figure 6.7.

This setup serves a dual purpose: driving the IGBT gates and implementing the selectors denoted as SxA in the schematic. Figure 6.7 provides an illustration of a selector between 15 V and GND, utilized as the IGBT gate driver. Variations in configuration are achievable by changing the connections to the emitter and collector of the BJT. When the Arduino pin's digital output is set to HIGH, the BJT activates, grounding its collector connected to the IGBT gate, thus turning the IGBT off. Conversely, setting the Arduino's digital output to LOW deactivates the BJT, allowing the system to link the 15 V power supply through a resistor to the IGBT gate, thereby turning it on (provided the IGBT emitter maintains a sufficiently low voltage). By utilizing Arduino and these simple schematics, precise timings can be assigned to each Pattern, and the desired LED pattern can be selected. This simplifies the detection of failures within the system.

To effectively monitor and store the voltages across each pattern, we employed an Arduino as a Data Acquisition System (DAQ). Its analog input pins were connected through a voltage divider to the test points highlighted in yellow in Figure 6.8. I utilized PLX DAQ

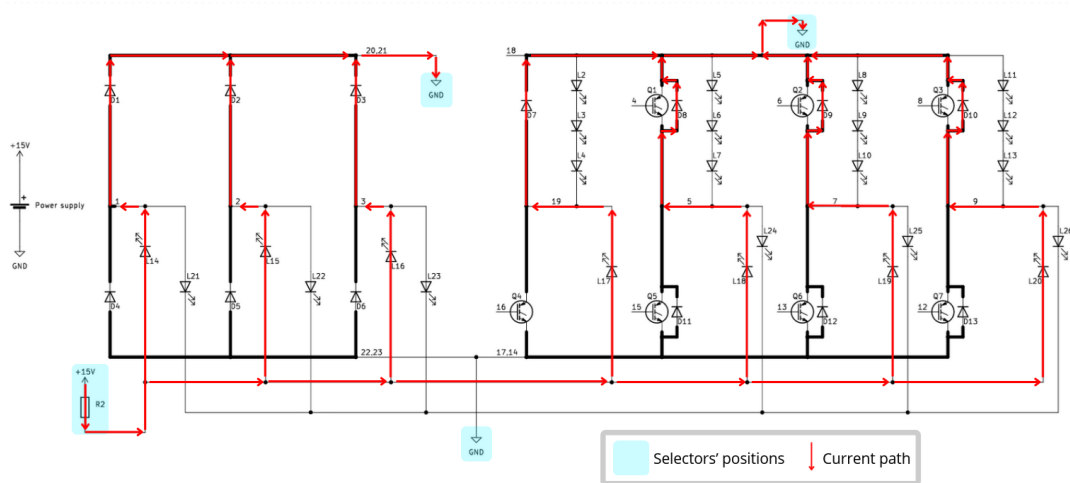


Figure 6.6: Simplified schematic for Pattern 8: all the diodes and LEDs crossed by the red arrows are turned on. Some selectors are not shown as they just act as open circuits.

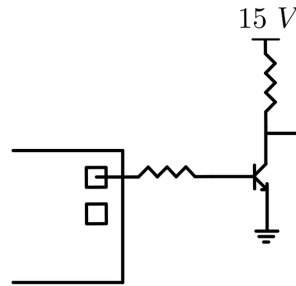


Figure 6.7: IGBT gate driver implementation with Arduino DUE

(Parallax Data Acquisition), a software tool developed by Parallax Inc., which facilitates data acquisition from microcontrollers like the Arduino directly into Microsoft Excel. This tool allows users to capture, log, and visualize data in real-time within Excel spreadsheets via Serial port communication. Thus, in addition to visually observing unusual LED patterns caused by failures, it was also possible to effectively demonstrate fractures through the derived plots.

To size the components, some simple rules have been adopted. The first one was consequent to the necessity of avoiding an excess of power across the resistors. At worst case, the resistors, rated for 0.6 W, needed to sustain 15 V, resulting in a value of resistance that needs to satisfy:

$$P = \frac{V^2}{R} < 0.6 \text{ W} \Rightarrow R > \frac{P}{V^2} = \frac{(15 \text{ V})^2}{0.6 \text{ W}} = 375 \Omega \quad (6.2)$$

Following this requirement, the sizing procedure proceeded to determine the appropriate

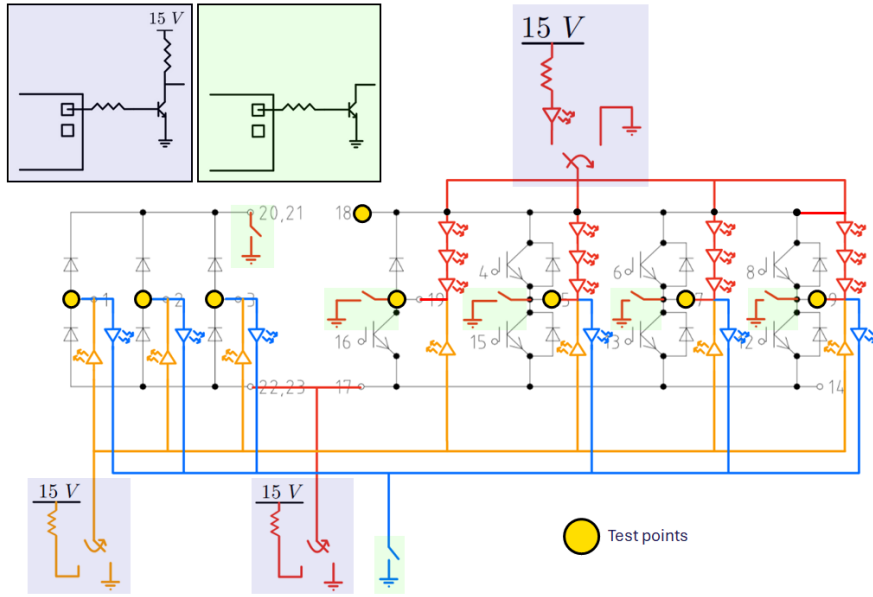


Figure 6.8: Monitoring circuit's test points

values for the collector and base resistors of the BJTs employed as IGBT gate drivers (refer to Figure 6.7). The base resistor's function is to restrict the current flowing out of the Arduino digital pin. Meanwhile, the collector resistor allows the flow of current to the IGBT gate. Due to the low currents involved, there were no stringent demands on the resistances, hence they were selected as follows:

$$R_{base} = 17.8 \text{ k}\Omega \quad R_{collector} = 19.6 \text{ k}\Omega \quad (6.3)$$

The value of $R_{base} = 17.8 \text{ k}\Omega$ has been adopted not only for the IGBT gate drivers but also for all other BJT base resistors in the schematic. Conversely, sizing the collector resistors of selectors S1A, S6A, and S8A required a more detailed examination of the current consumption of each LED and the voltage drops across various components. The voltage drop for both the inverter diodes and the rectifier diodes was found to be around $V_{d1} = 1.7 \text{ V}$ from the datasheets, while for the brake chopper diode around $V_{d2} = 1.05 \text{ V}$. The red LEDs have a voltage drop of around $V_{red} = 1.9 \text{ V}$, while the green ones (used for their higher voltage drop in the series parallel to the IGBTs in the inverter) around $V_{green} = 2.2 \text{ V}$. For S1A, the Kirchhoff Voltage Law (KVL) while the circuit is correctly operating, accounts for the voltage drop across resistor R1, LED L1, and the ON voltage drop of the IGBT, which has been taken equal to $V_{IGBT} = 4.5 \text{ V}$. As a result, to guarantee a current across the LED of 6 mA, it is derived:

$$15 V - R_1 I - 1.7 V - 4.5 V = 0 \Rightarrow I = \frac{15 V - 1.7 V - 4.5 V}{R_1} = 6 \text{ mA} \quad (6.4)$$

$$R_1 = 1466.7 \Omega$$

Therefore:

$$R_1 = 1.5 \text{ k}\Omega \quad (6.5)$$

Of course, if one component fails, given the increase in the voltage drop (due to the series of the three LEDs), the luminosity will decrease, but still remaining quite intense, so to assess the failure.

Regarding instead resistor R2, while the circuit is working, the KVL can be written as:

$$15 V - R_2 \cdot 7I - 1.7 V - 1.7 V = 0 \Rightarrow I = \frac{15 V - 1.7 V - 1.7 V}{7R_2} = 6 \text{ mA} \quad (6.6)$$

$$R_2 = 276 \Omega$$

Given also Equation 6.2, it has been decided to use the parallel of two 420Ω resistors, which guarantee a close enough resistance and a limited dissipated power.

Finally, for resistor R3, it goes:

$$15 V - R_3 \cdot 6I - 1.7 V - 1.7 V = 0 \Rightarrow I = \frac{15 V - 1.7 V - 1.7 V}{6R_3} = 6 \text{ mA} \quad (6.7)$$

$$R_3 = 322 \Omega$$

For simplicity, given again the power limitations, a single 420Ω resistor has been selected.

For prototyping simplicity, while a PCB is being designed, the circuit was assembled using a breadboard, and the preliminary tests were carried out through the setup shown in Figure 6.9. The complete setup is schematically shown in Figure 6.10 and its photos are instead shown in Appendix B, where the IGBT module is absent since it is inside the vibrating chamber.

During testing, each Pattern has been set to last 1 second. This results in a total testing time of 9 seconds, which equals to the worst-case scenario accuracy in failure detection. While this precision may seem excessive, it provides an ample margin of accuracy for the intended Expected Life measurements.

A Printed Circuit Board (PCB) was also designed to have a better setup for future works, and its schematic, created with KiCAD, is included in Appendix C. This PCB is intended to function as an Arduino DUE expansion board, providing a clearer LED view for monitoring the IGBT module compared to the breadboard setup.

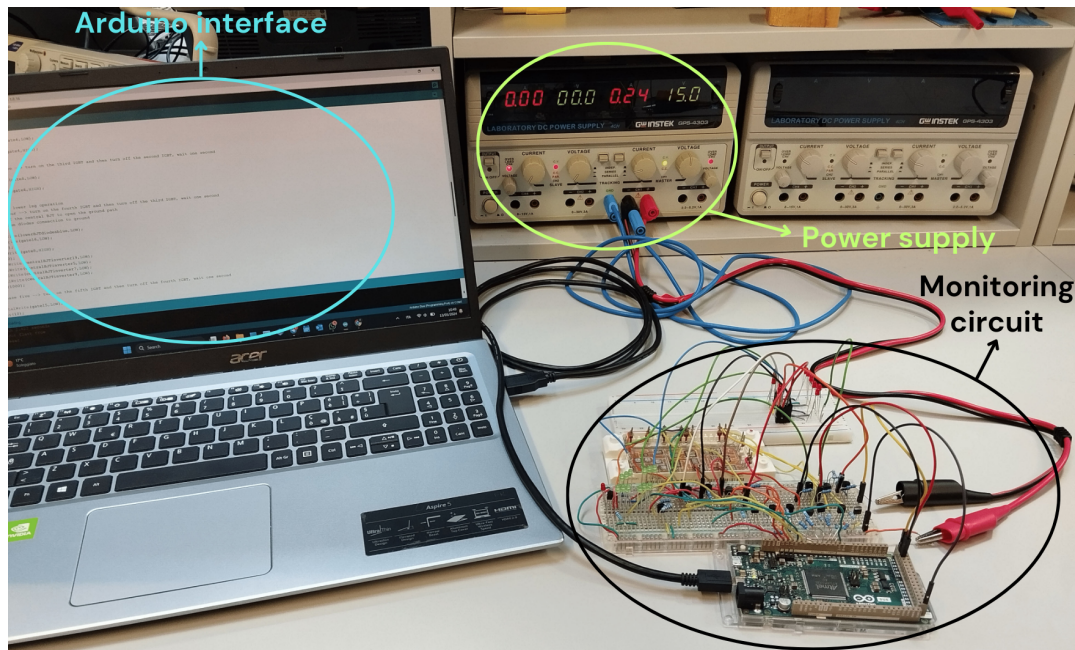


Figure 6.9: Laboratory experimental setup for circuit testing

6.4 Experimental results

As a starting point, each one of the seven configurations of the resonator has been tested for 20 minutes under a $10 g_{RMS}$ vibration, to verify that the structure was behaving correctly and was not showing any structural problems. As expected from simulation, the excitation was correctly propagating to the top of the resonator.

Subsequently, the tests involved maintaining the vibration for 30 minutes for each one of the seven configuration, inserting as input the equalized acceleration values reported in Table 5.2. While the module was excited, the monitoring circuit was actively checking its integrity. The same procedure was repeated for two different modules, starting from the least stressful condition (i.e., 7 stacked plates and $14 g_{RMS}$) and progressing to the most stressful condition (i.e., 1 stacked plate and $49 g_{RMS}$). The final results are reported in Table 6.2.

During the initial tests, no failures were observed in any of the modules for a number of stacked plates greater or equal of two (i.e., frequency higher than 3600 Hz). Failures were however observed after 20 and 25 minutes for the two modules under $49 g_{RMS}$ with one stacked plate.

The experimental results differ from the simulation ones, which predicted failures also with 2 and 3 stacked plates within a 30 minutes vibration. This discrepancy is explained by the properties of the silicone gel, which were not accounted for in the simulation, where a worst-case scenario was considered. After obtaining these outcomes, further literature research was conducted, focusing on the properties of silicone gel and its effects on exciting

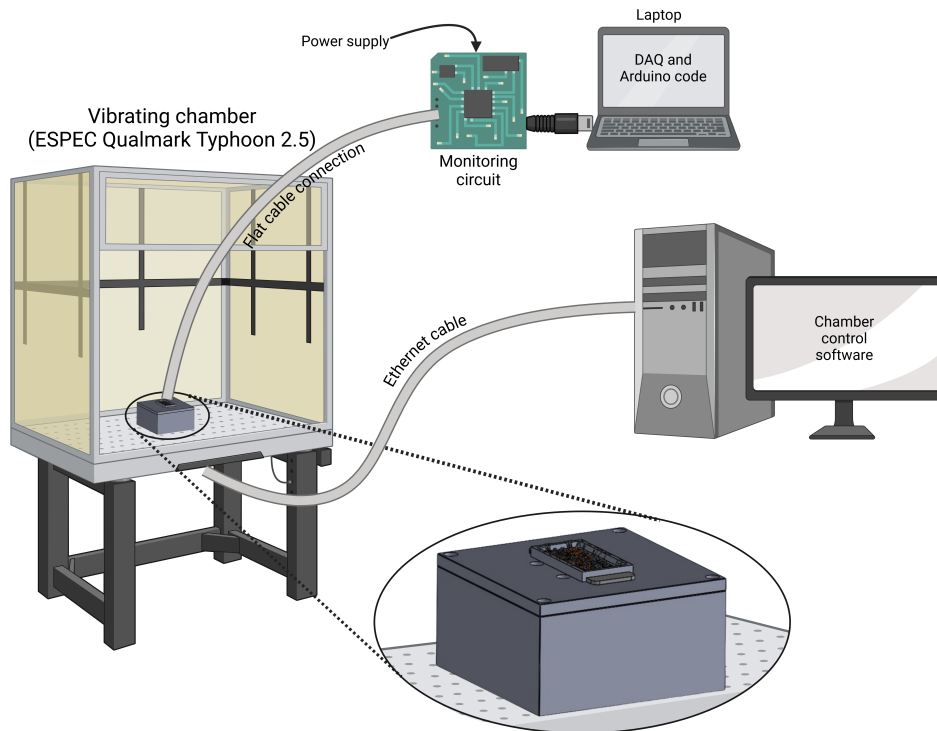


Figure 6.10: Experimental setup drawing

and attenuating certain vibration frequencies. Sasaki et al. [38] simulated bond wire strains in a silicone gel environment under random vibration excitation, highlighting that silicone gel attenuates higher frequencies, effectively acting as a low-pass filter. Therefore, while the resonator amplifies higher frequencies to approach the bond wires' resonance frequency, the silicone gel attenuates these frequencies, preventing failures. This characteristic is crucial for ensuring the reliability of IGBT modules under vibrating loads. By applying a silicone gel layer across the entire surface of the module, completely covering the bond wires, higher frequency excitations are cut off, maintaining proper module operation under vibration which are not too strong and with frequencies not too close to the bond wires' resonance ones.

When just one plate was stacked, and the vibration frequency was closer to the terminal bond wires' resonance one, failures were observed in all the modules and happened as cracks at their feet connected to the module's external pins. An image showing how the fractures happened is reported in Figure 6.11.

As expected from the simulations, the fractures happened exactly at the higher feet of the terminal bond wires. In particular, the bond wires failing were the gate loops. The failures were correctly identified from the circuit, which was showing strange LED patterns when failures happened. When strange LED patterns were identified, the vibration chamber was stopped and the module was visually monitored. Finally, a the voltages plot resulting from the employed DAQ system was analyzed, and is here reported for Module 3 in Figure 6.12,

Plates	f [Hz]	g_{RMS}	Module 1	Module 2	Module 3
7	1964.9	15	No failure	No failure	No failure
6	2149	17	No failure	No failure	No failure
5	2372.3	19	No failure	No failure	No failure
4	2652.8	23	No failure	No failure	No failure
3	3022.9	28	No failure	No failure	No failure
2	3548.1	35	No failure	No failure	No failure
1	4383	49	Failure (20 min.)	Failure (25 min.)	Failure (7.5 min.)

Table 6.2: Experimental results on IGBT modules with silicone gel

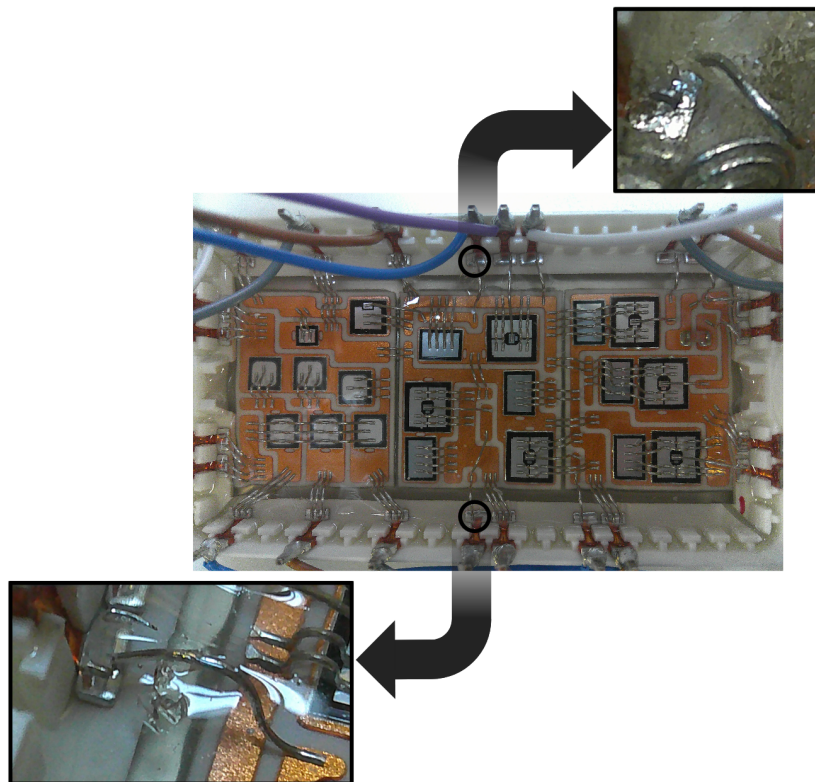


Figure 6.11: Full module in the center, failure on module 1 in the upper zoom, failure on module 2 in the lower zoom.

where the bond wire cracked as in Figure 6.13.

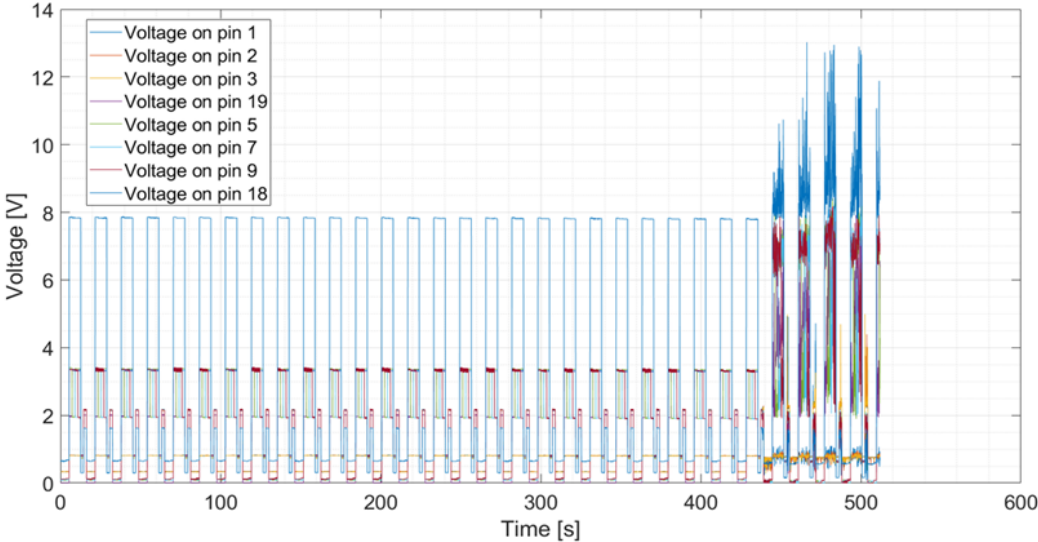


Figure 6.12: Voltages plot showing the crack after around 7.5 minutes

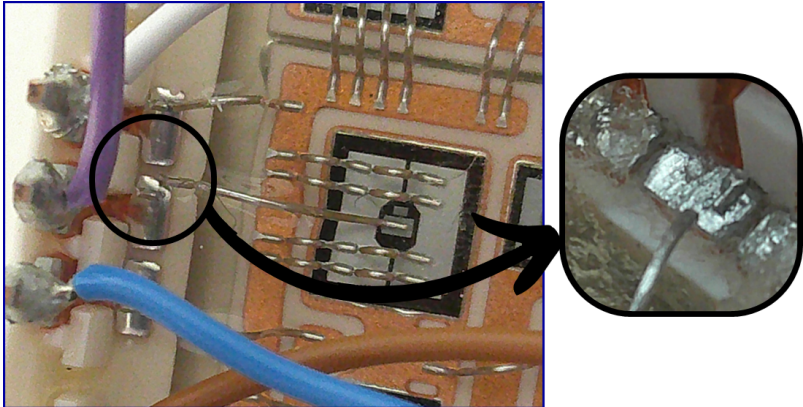


Figure 6.13: Crack on Module 3

Chapter 7

Results summary

Tests were conducted both in the ANSYS simulation environment and using Typhoon 2.5. The setup was identical in both conditions, consisting of a resonator with a certain number of stacked plates, with the IGBT module placed on top of the stack. This configuration allowed for the analysis of IGBT module reliability across frequencies ranging from 2 kHz to 5 kHz, while maintaining a constant displacement. This facilitated an assessment of bond wire reliability under different vibration frequencies. The results obtained from simulations did not account for the presence of silicone gel, which has been shown to strongly attenuate higher frequencies [38], thereby diminishing the resonator's amplification characteristics. Consequently, a difference between the outcomes in the two environments was observed. Table 7.1 presents the final results from both environments, where failures are observed within a 30 minutes random vibration excitation.

Plates	g_{RMS}	Sim. results	Experimental results		
			Module 1	Module 2	Module 3
7	15	No failure	No failure	No failure	No failure
6	17	No failure	No failure	No failure	No failure
5	19	No failure	No failure	No failure	No failure
4	23	No failure	No failure	No failure	No failure
3	28	Fail. (3.3 min.)	No failure	No failure	No failure
2	35	Fail. (15 sec.)	No failure	No failure	No failure
1	49	Fail. (< 1 sec.)	Fail. (25 min.)	Fail. (20 min.)	Fail. (7.5 min.)

Table 7.1: Final simulation and experimental results.

As shown in the summarizing table, differences between the simulation and experimental results are evident. These discrepancies are attributed to the silicone gel, which, as explained in the previous chapter, attenuates higher frequencies, thereby enhancing the reliability of

the IGBT modules.

However, the simulations accurately predicted the failure locations, identifying the terminal bond wires as the most fragile components. Importantly, the experimental work confirmed the simulation predictions regarding the failure cause, which is the presence of a crack. No lift-offs were observed, and there were no failures in the module dies. These results also confirm the findings of [39], where both temperature and sinusoidal vibration stress were combined to examine the Number of Cycles to Failure of a set of IGBT module samples.

Chapter 8

Conclusion

In conclusion, this thesis successfully expanded knowledge regarding the reliability of IGBT modules under vibrational stresses. Starting with a literature review, the most probable cause of failure was identified as potential cracks near the foot of the bond wires. Subsequently, an analysis was conducted on how to characterize random and harmonic vibrations, understanding their differences and how to relate them. Additionally, the thesis provided a theoretical background on their analysis techniques.

After introducing vibrating environments and their analysis methods, the focus shifted to studying basic mechanical properties, such as stress-strain relations, elastic modulus, Poisson's ratio, SN curves, and fatigue analysis. The Steinberg three-band method and Miner's rule were explained as they were adopted for assessing the expected life of the modules.

To ensure accurate simulation, the material properties of the IGBT module were analyzed, and the complete structure of the module, including its dimensions and mechanical properties, was summarized.

Before proceeding with the simulation, the ANSYS mechanical environment was explored using simple models to understand the correct boundary conditions for both harmonic and random vibration analyses. A precise 3D model of the IGBT module was developed, and initial simulations were conducted. Given that the thesis aimed to understand the parameters that most influence the expected life of these modules, a resonator was developed to relate random vibrations to harmonic ones. This approach allowed the use of random vibrating machinery in the laboratory with the resonator to examine the module's expected life dependence on excitation frequency. Alongside the mathematical derivation of a formula assessing the bond wires' first resonance frequency, the thesis demonstrated how the thickness, length, and shape of the wires influence their expected life. In particular, ANSYS simulations showed that terminal bond wires, being the longest, have lower first resonance frequencies, closer to real environmental vibration frequencies, making them the most likely to fail under vibrational loads.

Experimental work revealed that silicone gel significantly enhances the reliability of bond wires under vibrations by strongly attenuating high-frequency vibrations and acting

as a low-pass filter. Given that the resonance frequencies of the bond wires are relatively high (greater than 7 kHz), their stresses and strains are significantly reduced, and resonance effects are diminished. However, at frequencies close to the bond wires' resonance frequencies, failures were observed at the upper sides of the terminal bond wires' feet, consistent with simulation predictions. Consequently, this thesis recommends avoiding exposing the modules to vibrating environments with frequencies near the bond wires' resonance frequencies. Since a simple formula is provided to determine the bond wires' first resonance frequency, assessing the risk of failure is straightforward.

For future work, more extensive experimental tests could be conducted to fully validate the simulations. This would allow returning to the ANSYS environment to develop a more accurate model that includes silicone gel, enabling a wider range of tests (e.g., using different displacements). This approach could lead to deriving a fitted equation that determines the life of a module as a function of vibration frequency and displacement. Additionally, similar tests could be conducted for random vibrations without using a resonator, relating the module's life to different PSD curves.

Bibliography

- [1] ISO FDIS. 16750-3: 2023: Road vehicles-environmental conditions and testing for electrical and electronic equipment-part 3: Mechanical loads. *Geneva, Switzerland: International Organization for Standardization*, 2023.
- [2] Adam Niesłony, Robert Owsiański, and Artur Dziura. Methods of description of random loading in fatigue life calculation. volume 2028, page 020013, 11 2018.
- [3] Yanzhong Tian, Tong An, Fei Qin, Yanpeng Gong, Yanwei Dai, and Yanpeng Chen. Stress analysis of automotive igbt module under vibration load. In *2022 23rd International Conference on Electronic Packaging Technology (ICEPT)*, pages 1–4, 2022.
- [4] Y. Zhang, C. Zhan, L. Zhu, W. Wang, Y. Tang, and S. Ji. Investigation on failure mechanism of igbt modules under sinusoidal vibration. In *2022 Annual Meeting of CSEE Study Committee of HVDC and Power Electronics (HVDC 2022)*, volume 2022, pages 458–462, 2022.
- [5] Haojie Wang, Dongjing Liu, Yasong Fan, Yanchen Wu, Tieliang Qiao, and D.G. Yang. Modal analysis of igbt power devices based on ansys. In *2019 20th International Conference on Electronic Packaging Technology(ICEPT)*, pages 1–4, 2019.
- [6] Thomas Schriefer, Maximilian Hofmann, and Martin Maerz. Vibrational resistance investigation of an igbt gate driver utilizing frequency response analysis (fra) and highly accelerated life test (halt). In *CIPS 2018; 10th International Conference on Integrated Power Electronics Systems*, pages 1–6, 2018.
- [7] Vahid Samavatian, Armin Masoumian, Mehdi Mafi, Mostafa Lakzaei, and Davood Ghaderi. Influence of directional random vibration on the fatigue life of solder joints in a power module. *IEEE Transactions on Components, Packaging and Manufacturing Technology*, 9(2):262–268, 2018.
- [8] Huawei Wu, Congjin Ye, Yuanjin Zhang, Jingquan Nie, Yong Kuang, and Zhixiong Li. Remaining useful life prediction of an igbt module in electric vehicles statistical analysis. *Symmetry*, 12(8):1325, 2020.

- [9] MT Huber. Wlasciwa praca odkształcenia jako miara wyteżenia material. *czasopismo techniczne, leMBERG, austria*, vol. 22, 1904.
- [10] R v Mises. Mechanik der festen körper im plastisch-deformablen zustand. *Nachrichten von der Gesellschaft der Wissenschaften zu Göttingen, Mathematisch-Physikalische Klasse*, 1913:582–592, 1913.
- [11] Roderic S Lakes. Negative-poisson’s-ratio materials: auxetic solids. *Annual review of materials research*, 47:63–81, 2017.
- [12] Hasan Gercek. Poisson’s ratio values for rocks. *International Journal of Rock Mechanics and Mining Sciences*, 44(1):1–13, 2007.
- [13] Eric Stamper. Calculating fatigue in a random vibration environment. <https://www.linkedin.com/pulse/calculating-fatigue-random-vibration-environment-eric-stamper/>, 2017.
- [14] Ansys Innovation Courses. How to perform a Random Vibration Fatigue Analysis — Lesson 4. <https://courses.ansys.com/index.php/courses/random-vibration-analysis/lessons/how-to-perform-a-random-vibration-fatigue-analysis-lesson-4/>, 2024. [Online; accessed 10-May-2024].
- [15] Dave S Steinberg. Vibration analysis for electronic equipment. 2000.
- [16] Fp50r12kt4: 1200 v, 50 a pim three phase input rectifier igbt module. https://www.infineon.com/dgdl/Infineon-FP35R12KT4-DS-v02_00-en_de.pdf?fileId=db3a304316f66ee801174440e4132f81&intc=reco.
- [17] Qiang Huang, Cheng Peng, Serwaa Frimpong-Manso Ellen, Wenhui Zhu, and Liancheng Wang. A finite element analysis on the reliability of heavy bonding wire for high-power igbt module. *IEEE Transactions on Components, Packaging and Manufacturing Technology*, 11(2):212–221, 2020.
- [18] Daithi de Faoite, David J Browne, Franklin R Chang-Díaz, and Kenneth T Stanton. A review of the processing, composition, and temperature-dependent mechanical and thermal properties of dielectric technical ceramics. *Journal of Materials Science*, 47:4211–4235, 2012.
- [19] P Rama Murty Raju, S Rajesh, K Sita Rama Raju, and V Ramachandra Raju. Evaluation of fatigue life of al₂O₃/al₂O₃ particulate nano composite fabricated using stir casting technique. *Materials Today: Proceedings*, 4(2):3188–3196, 2017.
- [20] Matthew A Hopcroft, William D Nix, and Thomas W Kenny. What is the young’s modulus of silicon? *Journal of microelectromechanical systems*, 19(2):229–238, 2010.

- [21] Lin Zhang, Raymond Barrett, Peter Cloetens, Carsten Detlefs, and Manuel Sanchez del Rio. Anisotropic elasticity of silicon and its application to the modelling of x-ray optics. *Journal of synchrotron radiation*, 21(3):507–517, 2014.
- [22] Robert Edward Borocho. Mechanical properties and fatigue of polycrystalline silicon under static and high frequency cyclic loading. 2008.
- [23] Daan Hein Alsem, Olivier N Pierron, Eric A Stach, Christopher L Muhlstein, and Robert O Ritchie. Mechanisms for fatigue of micron-scale silicon structural films. *Advanced Engineering Materials*, 9(1-2):15–30, 2007.
- [24] Adarsh Basavalingappa, Ming Y Shen, and James R Lloyd. Modeling the copper microstructure and elastic anisotropy and studying its impact on reliability in nanoscale interconnects. *Mechanics of Advanced Materials and Modern Processes*, 3:1–10, 2017.
- [25] Wojciech Sas, Katarzyna Gabryś, Alojzy Szymański, et al. Determination of poisson's ratio by means of resonant column tests. *Electron. J. Pol. Agricu. Univ. EJPAU*, 16(03), 2013.
- [26] Yu-Bo Guo, De-Guang Shang, Xiao-Dong Liu, Chong-Gang Ren, Feng-Zhu Liu, Li-Hong Zhang, and Yu-Juan Sun. Recovery of fatigue damage and life prediction by laser irradiation healing treatment for copper film. *Journal of Materials Engineering and Performance*, 24:106–113, 2015.
- [27] TT Nguyen, D Yu, and SB Park. Characterizing the mechanical properties of actual sac105, sac305, and sac405 solder joints by digital image correlation. *Journal of Electronic Materials*, 40:1409–1415, 2011.
- [28] Y Zhou, M Al-Bassyouni, and A Dasgupta. Harmonic and random vibration durability of sac305 and sn37pb solder alloys. *IEEE Transactions on Components and Packaging Technologies*, 33(2):319–328, 2010.
- [29] John HL Pang, FL Wong, KT Heng, YS Chua, and CE Long. Combined vibration and thermal cycling fatigue analysis for sac305 lead free solder assemblies. In *2013 IEEE 63rd Electronic Components and Technology Conference*, pages 1300–1307. IEEE, 2013.
- [30] Cassandra Moers, Christian Dresbach, and Holm Altenbach. A fatigue lifetime prediction model for aluminum bonding wires. *Metals*, 13(10):1781, 2023.
- [31] Igc50t120t8rl: 1200 v power igbt chip. https://www.infineon.com/dgdl/Infineon-IGC50T120T8RL-DS-v02_01-EN.pdf?fileId=db3a3043382e8373013832d85bac4b85.
- [32] Idc28d120t8m: Fast switching emitter controlled diode for low / medium power modules. <https://www.infineon.com/dgdl/>

Infineon-IDC28D120T8M-DataSheet-v02_01-EN.pdf?fileId=5546d462576f34750157b78d596e2d68.

- [33] Mu-Tsang Chen and Ronald Harichandran. Statistics of the von mises stress response for structures subjected to random excitations. *Shock and Vibration*, 5(1):13–21, 1998.
- [34] Daniel J Segalman, Clay WG Fulcher, Garth M Reese, and Richard V Field Jr. An efficient method for calculating rms von mises stress in a random vibration environment. *Journal of Sound and Vibration*, 230(2):393–410, 2000.
- [35] Zhenzhen Shen, James Storey, Otto Fanini, and Michael Osterman. Modeling vibration induced fatigue failure of free standing wire bonds. In *International Symposium on Microelectronics*, volume 2017, pages 000635–000640. International Microelectronics Assembly and Packaging Society, 2017.
- [36] Huang-Kuang Kung, Bo-Wun Huang, and Hsiang-Chen Hsu. The effect of cross-section geometry of bonding wire on wire sweep for semiconductor packages. In *2010 5th International Microsystems Packaging Assembly and Circuits Technology Conference*, pages 1–4. IEEE, 2010.
- [37] Wikipedia. Six degrees of freedom — Wikipedia, the free encyclopedia. <http://en.wikipedia.org/w/index.php?title=Six%20degrees%20of%20freedom&oldid=1212791880>, 2024. [Online; accessed 09-May-2024].
- [38] Koji Sasaki and Nobutada Ohno. Fatigue life evaluation of aluminum bonding wire in silicone gel under random vibration testing. *Microelectronics Reliability*, 53(9-11):1766–1770, 2013.
- [39] Cao Zhan, Yaxin Zhang, Yizheng Tang, Francesco Iannuzzo, Lingyu Zhu, Shengchang Ji, and Frede Blaabjerg. Influence of temperature on bond wire fatigue of gate loops in igbt modules under sinusoidal vibration stress. In *2023 11th International Conference on Power Electronics and ECCE Asia (ICPE 2023-ECCE Asia)*, pages 1349–1354. IEEE, 2023.

Appendix A

Control software

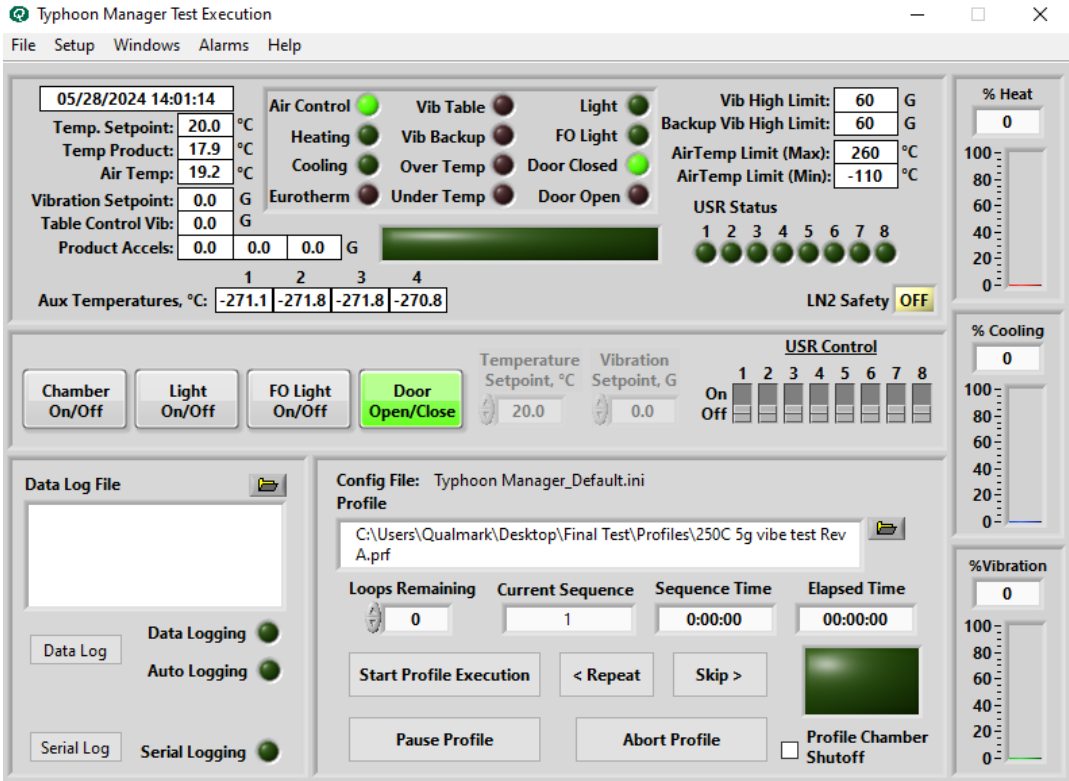


Figure A.1: Control panel for the Typhoon 2.5 control software

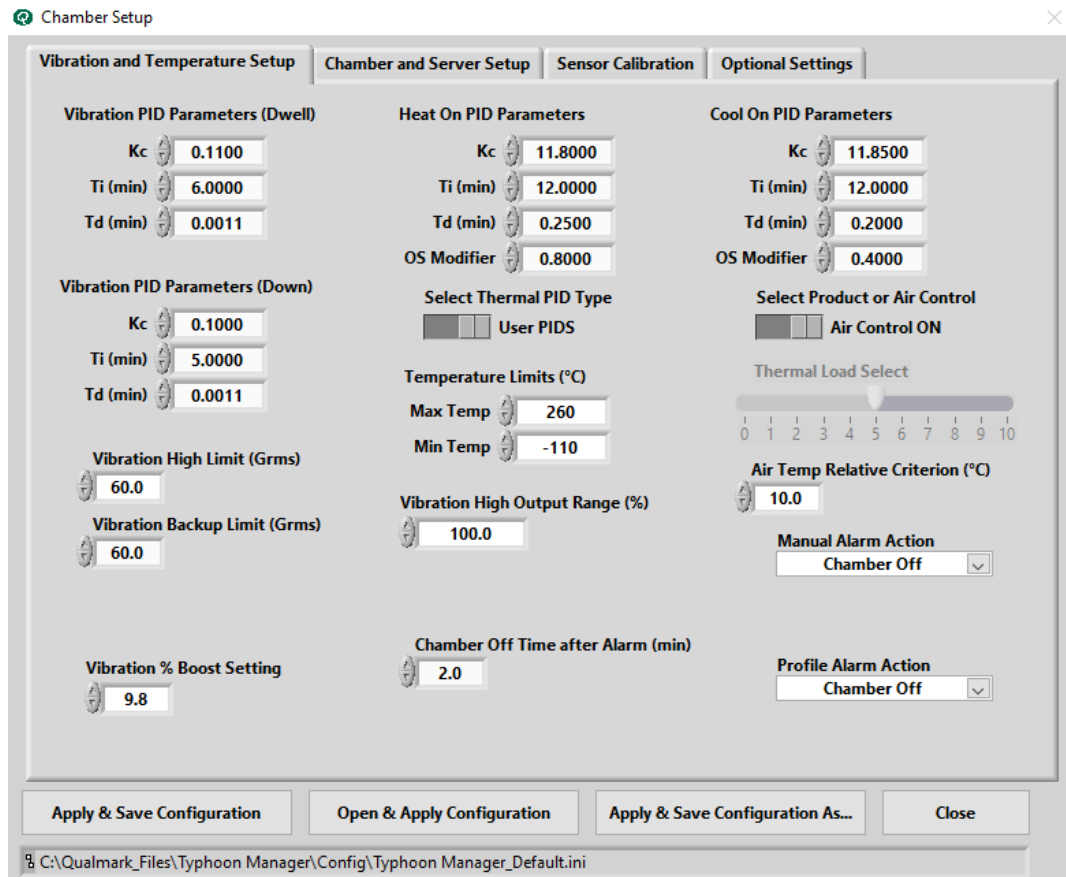


Figure A.2: Chamber setup in the control software

Appendix B

Experimental setup

Here are reported more comprehensive views of the resonator, when mounted on the ESPEC Qualmark Typhoon 2.5, and of the experimental setup.

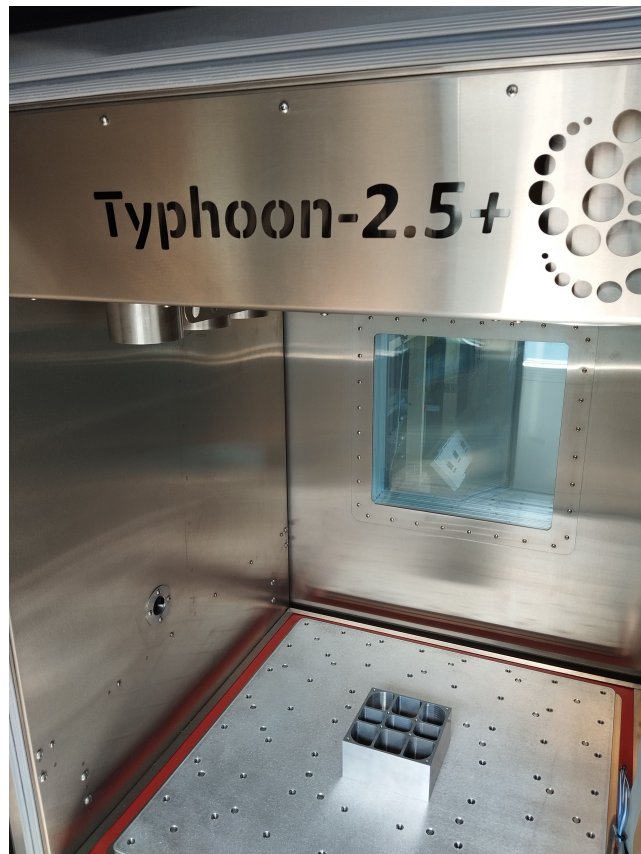


Figure B.1: Typhoon 2.5 and resonator base

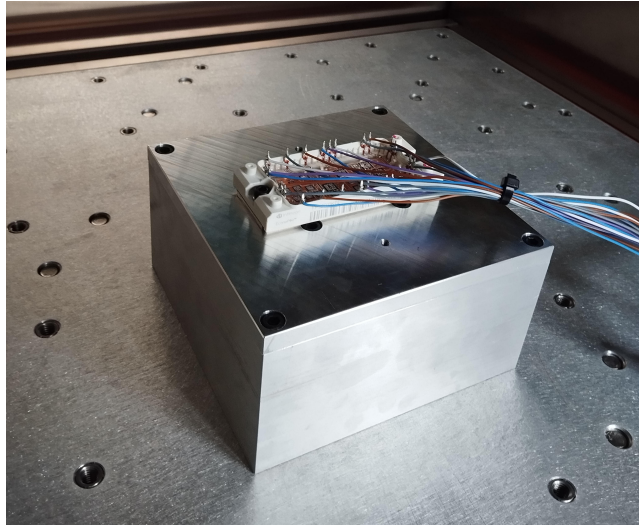


Figure B.2: Typhoon 2.5 and resonator with module



Figure B.3: Final laboratory setup for monitoring failures and managing the vibrating chamber

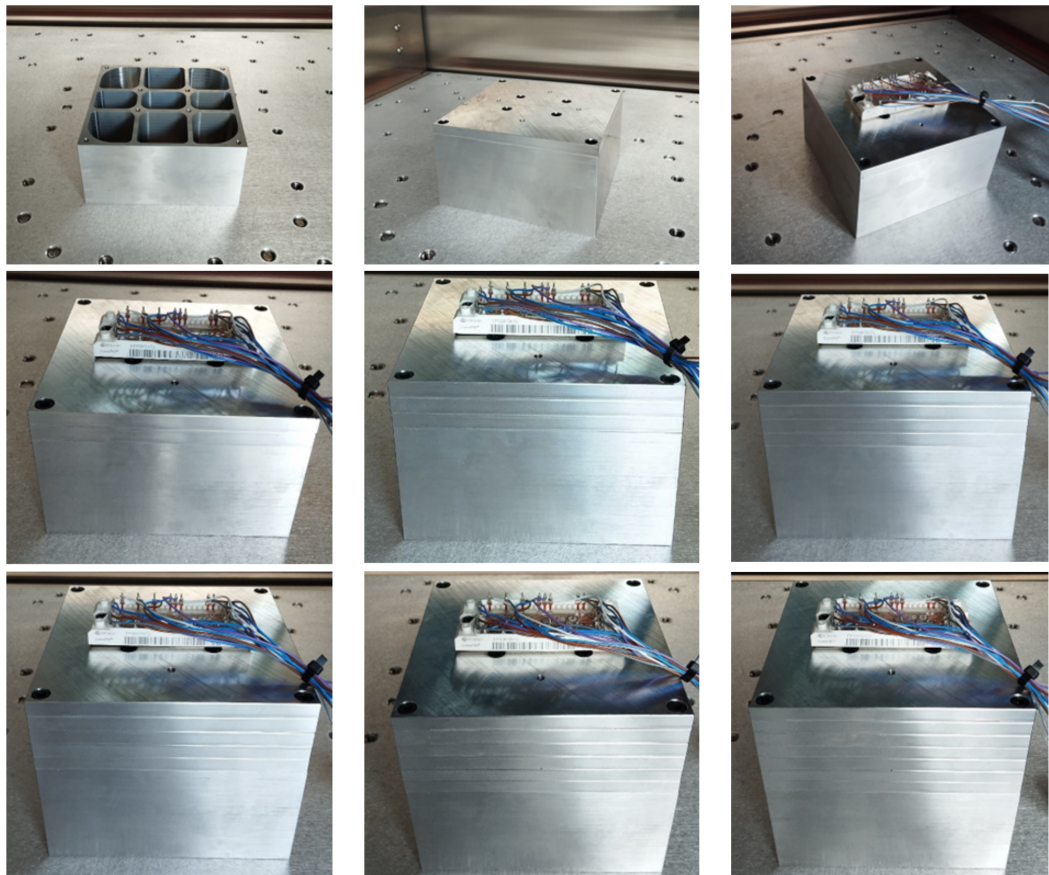


Figure B.4: Different resonator setup

Appendix C

Monitoring circuit

Here is reported the full schematic of the monitoring circuit.

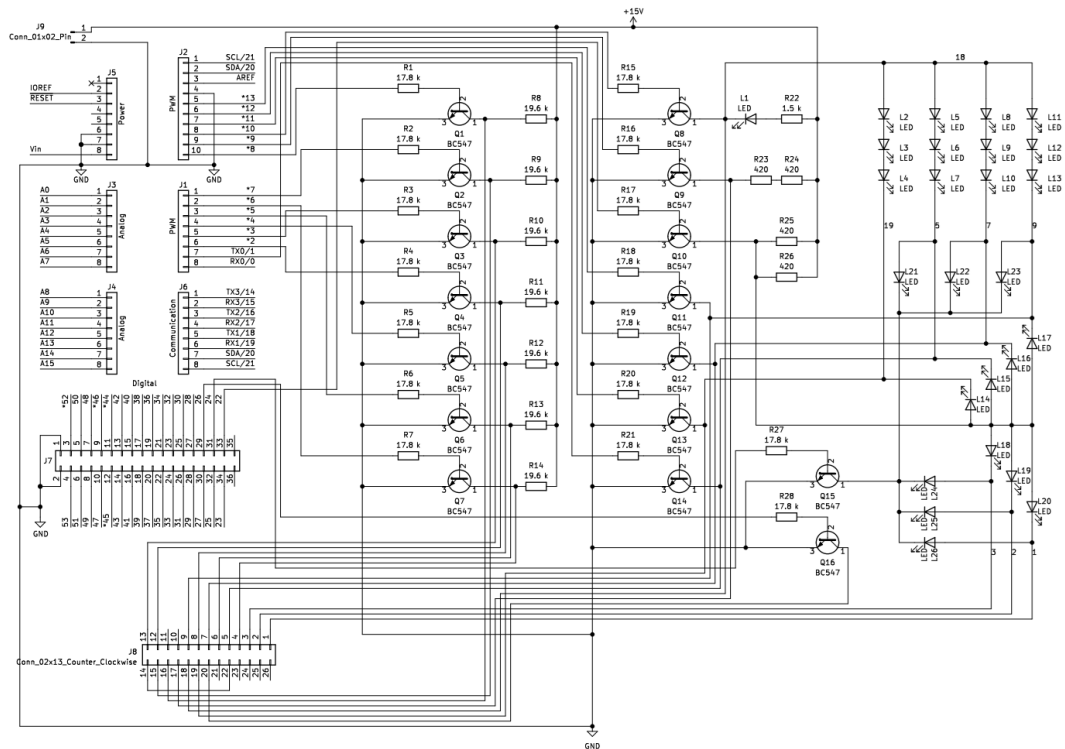


Figure C.1: Final monitoring circuit schematic, which just misses the data acquisition section